# Fluid flow through carbonate platforms as evidence for deep-seated reservoirs in Northwest Australia

Victoria Howarth, Tiago M. Alves*

3D Seismic Lab, School of Earth and Ocean Sciences, Cardiff University, CF10 3AT, United Kingdom

*Corresponding author (alvest@cardiff.ac.uk)

**ABSTRACT**

Fluid flow features in carbonate platforms of the outer Browse Basin, Northwest Australia, are investigated using 3D seismic and borehole data. During the Cenozoic, the study area evolved from a carbonate ramp to a rimmed platform with isolated carbonate build-ups; as such it played a key role in focusing fluid on their buoyant flow to the surface. Statistical analyses of direct hydrocarbon indicators show fluid flow to be focused in elevated areas i.e., the greater is the focusing of fluid, the larger is the carbonate platform or isolated build-up. Locally, karst systems created regions of enhanced permeability through the evolving carbonate stratigraphy. Karstified horizons are located on the top of carbonate build-ups and platform clinoforms as fluid buoyantly concentrates and diffuses up into topographic highs. In turn, the putative migration of gas and fluid generated hypogenic karst systems, enhancing permeability in otherwise lower permeability rock. Based on the interpreted data, we suggest a pivotal relationship between the presence of carbonate build-ups (and karsts) in the Browse Basin and hydrocarbon accumulations at depth. Areas of elevated topography focus sub-surface fluid, enhancing the permeability of carbonate successions. In turn, focused fluid flow can lead to the generation of methanogenic carbonates, enhancing the growth of isolated build-ups and leading to further generation of elevated features. This grants the identification of similar features on seismic data from Northwest Australia, and other Equatorial

margins in the world, as a valid proxy for the recognition of hydrocarbon accumulations below thick carbonate successions.

**Keywords:** Equatorial margins; Northwest Australia; carbonate platforms; carbonate build-ups; fluid flow; karsts.

## 1. Introduction

Equatorial margins with water temperatures above 20$^o$C are dominated by high organic productivity, resulting in the deposition of vast carbonate platforms (Testa and Bosence, 1999; Wilson, 2002; 2012). On these carbonate platforms, fluid-flow features and seafloor cold seeps are often linked to the presence of underlying hydrocarbon reservoirs or, instead, relate to the presence of significant volumes of methane and gas hydrates in near-surface strata (Hovland, 1990; Hovland et al., 1985, 1994; Série et al., 2012; Prinzhofer and Deville, 2013; Wenau et al., 2015). Cold seeps may stimulate abnormal 'oases' of biological activity, leading to growth of chemosynthetic communities that accumulate authigenic carbonates on the seafloor (Hovland and Judd, 1988; Hovland et al., 1994; Løseth et al., 2009; Dondurur et al., 2011). In the Porcupine (Southwest Ireland) and Vulcan (Northern Australia) basins, Hovland et al. (1994) have shown that focused seepage of hydrocarbons through the seabed is accompanied by higher-than-normal methane concentrations around growing mounds, with some degree of fault control on the mounds' position being accompanied by migration of hydrocarbons from sub-surface units. In the regions investigated by Hovland et al. (1994), deep-water carbonate build-ups are recognised at present in areas of substratum fluid flow.

The Northwest Shelf is the most important hydrocarbon province in Australia, with more than 5 billion barrels of oil and condensate and 152 Tcf of gas discovered since exploration began six decades ago (Longley et al., 2002). Most of these hydrocarbons are sourced from the syn-rift Plover Formation (Early-Middle Jurassic), which comprises the most important reservoir interval in the region (Longley et al., 2002; Tovaglieri and George, 2014). Hydrocarbon migration through carbonate units has been observed in the nearby Yampi Shelf (O'Brien et al., 2005) and in the Petrel sub-basin (Nicholas et al., 2014), but no detailed analysis of direct hydrocarbon indicators (DHIs) has been attained for the Browse Basin (Figs. 1a and 1b).

Through the interpretation of a high-quality seismic volume from Northwest Australia (Browse Basin), this paper aims to assess how valid is the mapping of hydrocarbon migration and seepage on an evolving carbonate platform as a method to identify deep-seated reservoirs and active petroleum systems (Figs. 1c and 2). The Cenozoic evolution of the Browse Basin records a change from a carbonate ramp setting to a rimmed platform with isolated build-ups (Figs. 2 and 3). Resulting changes in Eocene-Holocene stratigraphy had a significant impact upon seal competence above Mesozoic reservoirs. In this work, the spatial distribution of pockmarks, gas pipes and karst features are compared with the evolution of the imaged carbonate platform to corroborate their use as indicators of prolific hydrocarbon reservoirs at depth. With this in mind, this work aims to address the following research questions:

a) Is the distribution of DHIs in the Browse Basin related to the existence of deeper reservoir intervals?

b) Do fluid flow features focus in specific zones of the Browse carbonate platform, following features such as karstified areas, fault planes and platform margins?

c) Have the variations in sea level, currents and wave motion within this particular area of the Browse Basin impact upon the seal competence of Miocene units?

The paper starts with a detailed description of data and methods utilised, prior to the presentation of the geological, oceanographic and stratigraphic settings of the Browse Basin. We then describe in great detail the seismic stratigraphy of the study area. Growth rates of carbonate build-ups are quantified, and the distribution of karsts and DHIs analysed statistically. At the end of the paper are discussed: a) the oceanographic and tectonic controls on carbonate platform geometry in the Browse Basin and, b) the economic and environmental significance of the fluid flow paths identified on seismic data.

## 2. Data and methods

This work uses a 2850 km² 3D seismic volume from the Browse Basin, offshore Northwest Australia, and borehole data from two industry wells (Figs. 1c and 2). Seismic-borehole ties were based on chronostratigraphic, gamma-ray, resistivity and lithological data (ConocoPhillips, 2010). The Poseidon-1 well provided gamma-ray, ROP (rate of penetration) and resistivity data from 600 m to 4000 m below the seafloor, having crossed Upper Miocene to Middle Jurassic strata. The Poseidon-2 well provided lithological constraints below 2430 m i.e., for Cretaceous and Middle Jurassic units (ConocoPhillips, 2010).

The seismic survey was acquired in a direction parallel to the NW-striking continental shelf, and it is not aligned with the long axis of any studied fluid- venting structures or karst networks. Therefore, there is no spatial aliasing issues with the imaging of shallow features (Ho et al., 2012). For the intervals targeted in this study (Cenozoic) average peak-to-trough distance is 10-20 ms two-way time (TWT). Using a general velocity of 2.0 km/s, average peak-to-tough distances suggest a minimum vertical resolution of 5 m to 10 m. Interpreted horizons are relatively shallow (<2800 m), occurring at depths where data frequency and vertical resolution are remarkably preserved (Fig. 3).

Horizon mapping was performed every 20 inlines and crosslines, forming a grid of seed data for automated 3D auto-tracking, prior to converting the grid into a surface. Once computed, seismic attribute data were extracted from specific surfaces and in time-slices crossing the seismic volume. Seismic attributes used in this study include seismic trace (RMS amplitude) and seismic volume (variance) attributes. Amplitude maps display amplitude values at any given point across the interpreted seismic horizons, derived from the acoustic impedance of the strata (Brown, 2004).

‘Bright' and 'dim’ spots on amplitude maps are commonly associated with hydrocarbon accumulations; interpreters examine the map display to look for stratigraphic or structural controls on the presence of hydrocarbons (Hart, 1999).

Root-Mean Squared (RMS) amplitude maps show squared amplitude values for individual traces across a defined time window. These maps enhance high amplitude features and convert the dataset to positive amplitude values (Brown, 2004). Variance data quantify the differences between a given seismic trace and its neighbours. They highlight discontinuities in reflections and reduce interpretation bias as the mapping of single horizons is not required. Similar traces show low variance, whereas discontinuities have high variance and thus reveal the location of subtle stratigraphic features (Hart, 1999; Omosanya and Alves, 2013). Variance is useful for mapping the 3D offsets of features such as faults, therefore has strong applications for the karst, pockmark and pipe interpretation in this work (e.g. Marfurt and Alves, 2015).

### *2.1 Statistical analyses*

Calculations were run in Petrel® to quantify the area carbonate build-ups' surface area and volume. The area at each time slice was calculated and plotted as a function of depth. Seismically derived locations (points) for fluid-flow features and karsts were imported into ESRI ArcInfo 9.2®. Separate x,y files were extracted from Petrel® as data files from multiple time-slices. The data files were read in Global Mapper® and transformed into an elevation grid with a coordinate system that was exported as an Arc ASCII grid. This grid file was then loaded into Arc GIS® and subsequently exported as shapefiles in order that statistical analysis could be run.

The x,y data for karst and fluid flow features was extracted from Petrel® and loaded into Origin® to create a grid matrix. In order to do this a bin size had to be assigned considering the distribution and density of the data, as well as the extent of the study area. The bin area for the fluid flow features was 5 $km^2$ and for karsts was 4 $km^2$. A 2D frequency count generated a grid matrix following the specified bin constraints. Depth (z) values were assigned to the grid according to the number of points falling within each specified bin. These points were then manually converted into x,y,z columns in Microsoft Excel® and opened as grid data in Surfer®. A contour map was created for the grid, with colours assigned for discrete intervals to visualise and quantify the density distribution of the mapped features.

The spatial distribution of fluid-flow and karst features was analysed using the Nearest-Neighbour Analysis ($R_n$) package within ArcGIS®. The $R_n$ assesses whether the data is clustered, dispersed or randomly arranged (Fig. 4). The spatial statistics tool in ArcGIS® calculates the nearest-neighbour index based on the observed mean distance from each feature to its nearest neighbouring feature, and the expected mean distance for a hypothetical random distribution (Mitchell, 2005). This tool also calculates the distance between features and their nearest neighbour. In the $R_n$ package, a ratio of 1 represents a random distribution, a value <1 is clustered and a value >1 is dispersed (ESRI, 2013). The null hypothesis for the analysis is that features show complete spatial randomness (Fig. 4).

In order to answer the hypothesis of this study i.e., fluid flow features and karsts are not randomly distributed, a Z-score was calculated. The Z-score is a test for statistical significance which evaluates the normal distribution of the $R_n$ distances (ESRI, 2013). The test measures the standard deviation away from the mean. Very high or low Z-scores are found in the tails of the normal distribution curve indicating there to be little possibility an observed pattern is caused by chance (Fig. 4). When values sit within the significant ends of the curve, the null hypothesis may be rejected.

A Z-score was calculated for the entire data set, and then at individual horizons, selected for their stratigraphic significance following interpretation of the seismic data, to: a) understand which stratigraphic horizons were more clustered, and b) whether statistical results for the fluid flow features were similar to that of karsts.

## 3. Geological setting

### *3.1 Geological evolution of the Northwest Shelf*

The study area is situated in the central part of the Browse Basin, a NE-trending offshore basin covering 105,000km² of the Northwest Shelf of Australia (Stephenson and Cadman, 1994) (Figs. 1 and 2). The basin is bounded to the NW by the Scott Plateau, to the SW by the Rowley and Canning basins, and to the NE by the Vulcan sub-basin. It is separated from the continent by the Kimberley Block (Figs. 1b and 1c).

The Kimberley Block is a stable shield composed of Archaean and Proterozoic plutonic and metamorphic rocks that are overlain by deformed sediments and minor volcanics (Veevers, 1967; Stephenson and Cadman, 1994). During the Late Carboniferous, continental rifting opened a NE-trending trough near the present-day coastline of Western Australia (Powell, 1976; Longley et al., 2002). In the Lower to Middle Jurassic, the Northwest Australia continental margin started to develop following the rifting of Greater India from Australia (Langhi and Borel 2007; Rosleff-Soerensen et al., 2012). This second rifting episode caused the fragmentation of the Browse Basin into several fault-bounded NE-trending troughs, and was accompanied by intense volcanism (Bradshaw et al., 1994; Keall and Smith, 2004) (Figs. 2 and 3). Continental rifting formed four major sub-basins on the Northwest Shelf at this time - Yampi and Leveque to the south, Caswell and Barcoo in the centre and the Scott Plateau to the north – all showing predominant NE-SW structural trends that are still observed today (Rosleff-Soerensen et al., 2012) (Figs. 1b and 2).

The Early Cretaceous denotes a transition to a passive-margin setting (Stephenson and Cadman, 1994). In the study area, post-rift thermal sag generated widespread subsidence and regional flooding (Longley et al., 2002; Rosleff-Sorenson et al., 2012). A series of sedimentary basins were then structurally defined as margin parallel half-grabens, with thick passive-margin sediments of Late Jurassic-Early Cretaceous age burying the Middle Jurassic structural relief (Langhi and Borel

2007; Rosleff-Sorenson et al., 2012). This setting continued into the Paleogene, in which is recorded the deposition of clayey (marine) drift units (Figs. 2 and 3).

In the Early Miocene, oblique collision and partial subduction of the Australian Plate (and Papua New Guinea) under Southeast Asia resulted in shallow normal faulting and subsidence of the outer Northwest Shelf (Stephenson and Cadman, 1994). In the Browse Basin, these renewed tectonic stresses were oblique to syn-rift structures, resulting in soft-linkage of Neogene faults to basement structures. In contrast, faulting in the Bonaparte Basin was closely controlled by basement fabric (Harrowfield and Keep, 2005) (Fig. 1b).

### *3.2. Regional stratigraphy*

Stratigraphic units in the Browse Basin extend from Permian to Holocene (Figs. 2 and 3). Permian strata comprise fluvial claystones to siltstones, whereas Early-Middle Triassic sedimentation reflects a transition from marine shale and silt to Upper Triassic fluvio-deltaic to shallow marine sequences (Stephenson and Cadman, 1994). During the Early-Middle Jurassic epochs, a tidally influenced deltaic system (Plover Formation) evolved on the NWS, with prodelta units accumulating in the study area (Tovaglieri and George, 2014). Similarly to the Vulcan Basin, relatively thick evaporites may occur in the Paleozoic succession that underlies the Browse Basin, as revealed by a shelf-margin diapir developed close to the seafloor (see also Longley et al., 2002; Wu et al., 2016) (Figs. 5 and 6). Above the Palaeozoic succession, syn-rift sandstones form the major reservoir interval in the basin (Tovaglieri and George, 2014) (Fig. 5).

The final phase of rifting in the Middle Jurassic generated the NE-SW structural trends observed, and a basinwide unconformity associated with a regional uplift episode (Rosleff-Soerensen et al., 2012). In contrast, post-rift thermal sag during the Early Cretaceous caused increased subsidence in the centre of the Browse Basin. At this time, thick organic-rich marine sediments were deposited in a series of long-lived sedimentary basins (Stephenson and Cadman, 1994; Rosleff-Soerensen et al., 2012). The majority of these basins comprised margin parallel half-grabens, with thick passive-margin sediments burying the Middle Jurassic structural relief (Langhi and Borel 2007; Rosleff-Soerensen et al., 2012).

In the Paleocene, sedimentation shifted to argillaceous carbonates (Apthorpe, 1988). Later in the Oligocene, a pronounced stratigraphic break is recorded across the basin in association with uplift and erosion over most of the inner shelf (Stephenson and Cadman, 1994). Subsequent reactivation of Jurassic and older fault trends during the Early Miocene led to subsidence of the outer shelf, and deposition of thick prograding carbonate units (Stephenson and Cadman, 1994) (Figs. 2 and 3).

In the study area, depositional systems evolved from an Eocene-Lower Miocene carbonate ramp to a rimmed platform comprising tropical reefs during the Middle-Late Miocene (Apthorpe, 1988; Longley et al., 2002; Rosleff-Soerensen et al., 2012). This abrupt change was accompanied by an eustatic sea-level fall of 50±5 m, causing a shift to very shallow carbonate facies and localised sub-aerial exposure (Haq et al., 1987; Apthorpe, 1988; Cathro and Austin, 2001; John et al., 2004). A prominent seismic unconformity was then formed across the neighbouring Bonaparte Basin (Marshall et al., 1994). The Browse Basin platform was subsequently drowned under thick hemipelagic sedimentation in the Late Miocene, up to the present day (Rosleff-Soerensen et al., 2012).

### *3.3 Physiography, climate and oceanography*

Seafloor morphology in the outer Browse Basin reveals a smoothed profile (Fig. 5). The shelf strikes NE with a very low gradient, up to a water depth of ~500 m. In the study area, a salt diapir pierced through the distal part of the shelf. Selected seismic profiles show the diapir to penetrate strata older than the Cretaceous (Fig. 6c).

At present, the Köppen climate classification for Northwest Australia is Aw, a savannah climate (Peel et al., 2007). The study area is subject to seasonal storm events, with the largest storm waves being associated with tropical cyclones (Lees, 1992). The oceanography of the Northwest Shelf is also affected by the South Equatorial Current, which is driven by easterly trade winds and by the Indonesian Troughflow, or ITF (Fig. 7a). The ITF circulates on the Northwest Shelf, with warm low-salinity waters from the North Pacific delivering larvae of Pacific and Asian reef species to the shelf. It subsequently affects the biological structure of modern reefs (Heyward et al., 1997; Collins, 2010).

The Leeuwin Current flows SW along the Northwest Shelf, with weaker occasional NE-flowing currents introducing cold deep-water onto the continental shelf (Holloway and Nye, 1985) (Fig. 7a). Areas of the Browse Basin swept by strong currents and intermittent tropical cyclones favour the deposition of coarse-grained seafloor sediments (O'Brien et al., 2005). In addition, the Northwest Shelf has strong baratropic, semi-diurnal tides (Holloway et al., 2001; Van Gastel et al., 2009). The large tidal forcing, density stratification of the waters and steep complex 3D topography in the Browse Basin produces a complex internal wave climate, which is strongest where tidal flow is directed at steep isobaths (Rayson et al., 2011).

### *3.4 Carbonate platform classification*

In this work we follow a classification of carbonate platforms based on their external morphology. Bosence (2005) suggests the overall morphology, size and stratigraphic evolution of carbonate platforms to be primarily controlled by basinal or tectonic setting. Smaller scale platform features (grain type, facies and depositional sequence) are controlled by biotic evolution, sea-level history and climatic factors. Carbonate ramps are gently sloping (<1°) shallow wave-agitated facies of the nearshore which change downslope into deeper low-energy deposits (Ahr, 1973). Ramps lack continuous reef trends or significant sediment gravity-flow deposits. They are composed of nearshore skeletal shoal complexes, ooids and tidal flat carbonates, and distal argillaceous wackestones and mudstones with open-marine biota (Read, 1985).

Rimmed carbonate platforms exist in shallow seas with a pronounced increase in slope, particularly on wave-agitated shelf-edges (Read, 1985). The continuous rim formed along the platform margin restricts circulation and wave action to form low-energy lagoons within the platform (Ginsburg and James, 1974). On their aggradational-progadational fringes, depositional facies grade from the inner platform to deep-water in a predicted sequence of coastal and lagoonal siliclastics, tidal flat carbonates, skeletal or oolitic sands, patch reefs, skeletal sands, reef-derived rudites, depth-zoned reefs, peri-platform sands, breccias, turbidite shales, deep-water pelagites, distal turbidites and shales (Read, 1985). Wind-oriented reefs develop stronger growth and cementation, whilst the leeward side of reefs form a pronounced talus (Schlager, 2005)

Drowned platforms occur where subsidence or sea-level rise exceeds up-building by biological production of carbonate sediment. Deposition thus switches to basinal hemipelagic facies whenever platform drowning occurs (Read, 1985). A major landward shift occurs in the shallow platform facies and there is a vertical transition from shallow to deep-water facies, occurring either abruptly or gradationally, revealed on seismic data by a typical back-step geometry (Read, 1985).

## 4. Results

### *4.1 Seismic-stratigraphic units*

The nature and geometry of seismic reflections allowed us to interpret significant changes in paleoenvironment within the Browse Basin. Therefore, Jurassic to Holocene strata has been divided into six (6) units based on the correlation of key seismic horizons with Poseidon-1 and Poseidon-2 wells (Figs. 5 and 8).

#### *4.2.1 Unit 1: Cretaceous to Eocene*

Unit 1 is bounded by BB0 and BB1 and is Cretaceous to Eocene in age (Fig. 5). The unit is 568 m-thick at the location of Poseidon-1 (Figs. 6a and 6b). A key characteristic is that an asymmetrical channel incises the continental shelf, showing a typical cut-and-fill geometry (Fig. 6a). By the end of Unit 1, the channel changes into a series of multiple incisions developed on the shelf break of the early carbonate ramp. The high-amplitude fill of these incisions, relative to the fill of the older channel, indicates higher energy conditions and the transport of coarser sediments onto the ramp margin.

Wireline data for Poseidon-1 show gamma-ray values to fall and gas readings to increase at 3960 m; the shallow resistivity log increases and the deep resistivity decreases giving a high separation. This is typical of a porous water saturated formation. Brief peaks in the deep resistivity surpassing shallow resistivity resemble pockets of gas. For the rest of Unit 1 the gamma-ray values increase and resistivity lines overlie, showing an impervious nature. The gas levels continue to fluctuate showing gas to be irregularly distributed within the matrix of the formation.

#### *4.2.2 Unit 2: Eocene*

Unit 2 is bounded by BB1 and BB2 and is Eocene in age (Fig. 5). Unit 2 is 1045 m-thick at Poseidon-1 (Figs. 6a and 6b). The lithologies crossed are predominantly calcilutite grading upwards to argillaceous calcilutite and marls (Fig. 3).

Seismic profiles and variance slices show numerous channel incision surfaces in the lower half of Unit 2 (Fig. 6b). The morphology of incision surfaces and the presence of calcareous marls in cores are diagnostic of tidal inlets (Fig. 9a). They form perpendicular to the slope and indicate tidal forcing of SE-driven currents (Fig. 6b). Towards the top of Unit 2 incisions are infilled and a more defined shelf-break develops (Figs. 8a). Clinoforms prograde more than 10 km to the NW, but over time these begin to aggrade on the ramp top (Fig. 8a).  With aggradation on the ramp top, incisions are replaced by conformable, continuous reflections (Figs. 8a and 9b).

At the top of Unit 2, a retrograding wedge is seen retreating to the top of the ramp. Poseidon-1 shows the resistivity lines to overlie and total gas levels remaining steadily low for the remainder of Unit 2. This character is suggestive of low permeability strata with little gas present.

*4.2.3 Unit 3: Eocene-Oligocene*

Unit 3 is Late Eocene to Oligocene in age, and bounded by BB2 and BB3 (Fig. 8a). Unit 3 is 430 m-thick at Poseidon-1. Clinoforms develop above a retrograding wedge at the top of Unit 3, showing a progradation of ~19 km (Figs. 8a and 8b). In the distal region of the ramp are observed four sequences of prograding clinoforms with foresets up to 225 m high, downstepping by ~90 m (Figs. 8b and 10a). The foresets are characterised by reflections with variable amplitude, and decreasing continuity, as they advance out into the basin (Fig. 10a).

In proximal areas of the ramp, a high-amplitude unconformity separates sub-parallel reflections from chaotic to transparent seismic facies (Figs. 8a and 10b). In more distal areas, the bedforms of prograding wedges are truncated by the Oligocene unconformity (Figs. 8b and 10a). Variance maps show dendritic forms diagnostic of carbonate karst structures on the SE end of the ramp top (inset in Fig. 11).

Wireline data from Poseidon-1 show a similar character to Unit 2. At 2300 m gamma values are low with a sudden jump in the deep resistivity values with shallow and deep separation. This would imply a permeable clean formation with the presence of gas. For the rest of Unit 3, the resistivity curve suggest low permeability. Sharp peaks in shallow resistivity record karst features, creating localised permeability streaks.

*4.2.4 Unit 4: Miocene*

Unit 4 is bounded by BB3 and BB4, and is Miocene in age (Figs. 5 and 8c). The Poseidon-1 well crossed 1030 m of strata belonging to Unit 4 (Figs. 6a and 6b). A prograding front in Unit 4 back-steps to the position of the T1 prograding wedge in Unit 3 to form a gently dipping carbonate ramp (Fig. 10a). After advancing 24 km to the NW, the gently dipping ramp evolves into a rimmed carbonate platform during the Middle Miocene. This change is marked by thick aggradation, with a topographic lip at the break of slope separating the rimmed platform from onlapping basinal and slope sediments (Fig. 8c).

The chaotic nature of seismic reflections at the platform margin is diagnostic of carbonate sediments. Behind the platform margin, chaotic karst horizons with mounded geometries change into horizontal continuous reflections (Fig. 8c). Carbonate mounds on the platform top develop up to 17 km landwards of the platform break. These mounds spread across 20 km, and are onlapped from the SE by more proximal sediments (Figs. 12 and 13a). This juxtaposition of facies is recorded by a lateral change from chaotic carbonate build-ups to inclined onlapping continuous reflections (Fig. 12a).

The variance map from the top of Unit 4 shows carbonate build-ups with karstification limited to the elevated tops of the build-ups (Fig. 11). The carbonate build-up at the proximal platform is onlapped before BB4, and lacks karst features (Fig. 11). RMS amplitude data for Unit 4 show the highest amplitudes on the more proximal area of the platform, a character suggesting changes in physical properties of the sediments with paleowater depth (Fig. 13a). Wireline data for Poseidon-1 shows the shallow and deep-resistivity curves to overlie across most of Unit 4, with occasional small separations, revealing intervals of higher permeability. There are frequent variations in resistivity values, indicating a scattered distribution of formation fluid. Gamma-ray values are low, typical of a carbonate succession.

*4.2.5 Unit 5: Pliocene to Holocene*

Unit 5 is bounded by BB4 and the seafloor (Fig. 5). BB5 is an intermediate surface above which a karstified succession is observed close to the seafloor (Figs. 5 and 6c). Unit 5 is 552 m thick at Poseidon-1, but its thickness increases on the continental slope to the NW. The unit is composed of continuous internal reflections, which initially onlap the palaeotopography behind the platform edge until it is smoothed out (Fig. 5). Beyond the slope break, wedges of strata eroded from the carbonate platform onlap the margin as a debris apron (Figs. 5 and 8c). Sediment thickness in Unit 5 is lower above the Miocene platform and isolated build-ups, showing that the carbonate geometries continue to influence modern-day deposition.

Wireline curves from Poseidon-1 show a large increase in gamma-ray values from Unit 4 into Unit 5. Gamma-ray values fluctuate at a high frequency, demonstrating the heterogeneous nature of the sediments. Resistivity values highlight the poor permeability of hemipelagites composing Unit 5.

**5. Middle to Late Miocene isolated carbonate build-ups**

Isolated carbonate build-ups (ICBs) have been recorded from -1050 to -1750 ms (Figs. 12 and 13). They are typically 1 km to 16 km wide and form across the extent of the carbonate platform. The outlines of the build-ups have been vertically stacked in Fig. 13b to visualise the spatial shifts in their growth. They are also identified in key horizons in Fig. 14.

The ICBs appear for the first time at a depth of about -1750 ms as four isolated build-ups formed in the NE corner of the study area (Fig. 14a). Approximately 100 ms above these first build-ups are observed multiple, but smaller, build-ups on structural and variance data (Fig. 14b). These larger ICBs do not form directly above the first set of carbonate build-ups; instead have shifted up to 10 km towards the SW (Fig. 14b and 14c). At -1450 ms, a second nucleus of build-ups develops to the SW, behind the platform margin (Fig. 14d).

At -1350 ms, carbonate production occurred preferentially in the NE and SW corners of the study area, with a distinct gap in the centre (Fig. 14e). Towards the end of the Miocene, the ICBs start to disappear with onlap of more homogeneous parallel strata. The ICBs in the more proximal SW region are drowned at -1150 ms. Those ICBs in the NE continue their growth to -1050 ms before their quick demise (Figs. 14f to 14h).

*5.1 Carbonate growth patterns*

Carbonate growth throughout the Miocene has been quantified on seismic data through the calculation of the 2D surface area of carbonate build-ups. When plotted on a graph, the data show a two-stage pattern (Fig. 15). Initially carbonate growth is low with only 59.42 km² of ICBs. This value doubles within 100 ms as lots of smaller build-ups appear (Fig. 15). Carbonate growth increases up to -1150 ms, revealing both an increase in 2D area and number of ICBs. At -1150 ms the growth levels peak with the largest build-ups being observed in the NE and SW. Growth falls by 2/3 over 100 ms above -1150 ms, as the build-ups in the SW cease to grow first. By -950 ms TWT the carbonate factory was ended and the ICBs drowned beneath the hemipelagites in Unit 5 (Fig. 16).

The carbonate growth at each build-up site is limited to increasingly smaller areas towards the Late Miocene (Fig. 17). This suggests the platform to be in its keep-up phase with sufficient accommodation space available only in deeper waters, a setting enhancing the rim morphology on the platform. The gentle slope on the SE edge represents the debris apron of the leeward side (see Discussion section).

A different explanation relates to the role of bottom currents in the evolution of the carbonate build-ups in this work, a factor well documented in the Maldives (Betzler et al., 2009; 2013 Lüdmann et al., 2013). These authors proposed that the Pliocene drowning of the Maldives's carbonate platform was controlled by monsoon-driven currents. In this case, the onset and relative intensification of the monsoon during the Neogene caused the drowning of the Maldives platform through the increase of available nutrient into surface waters (Betzler et al., 2009). In a setting dominated by convergence between Australasia and Indonesia, and subsequent deepening of the NW Australia margin from the Late Miocene onwards (Rosleff-Soerensen et al., 2016), a similar phenomenon to that recorded in the Maldives cannot be discarded. Progressive upwelling of ITF waters on the continental shelf may have drowned the Miocene carbonate platforms, leading to the deposition of hemipelagites in Unit 5 on a continental margin recording gradual subsidence. This setting is further discussed in Section 9.1.

*5.2 Karsts and sinkholes*

On vertical seismic profiles, karst systems are characteristically chaotic, producing a rugged topography (Fig. 11). On variance time-slices, the karsts display a typical negative relief and are 10's to 100's m across (Fig. 18a). The first karst event extends from -1700 to -1900 ms, from near the base Oligocene unconformity (BB1) into the Early Miocene (Figs. 18b and 19). The rounded cavities and branched karsts change from being localised on the ramp top at -1900 ms, to a more pervasive pattern across the entire ramp at -1750 ms i.e., in the lower part of Unit 4 (Fig. 18a). Sub-circular sinkholes are diagnostic of dissolution by groundwater, indicating subaerial exposure of the shelf top and a basinward shift of the regional meteoric lens. However branched forms appear too, suggesting rising thermal waters altered the carbonates simultaneously, forming hypogenic karsts (Fig. 18a).

At -1700 ms, karst depressions move away from the inner ramp area and concentrate above the prograding clinoforms, which form the first slope break (Fig. 19). These karsts are branch-like with irregular tunnel forms, suggesting they were generated below the surface in meteoric-vadose conditions. The preferential development of karsts at the prograding front likely relates to the migration of diagenetic fluids to the ramp edge. Above the karst systems, a high-amplitude continuous reflection indicates fine-grained deposits to have replaced the chaotic carbonate facies on the inner ramp (Fig. 19).

Seismic profiles and variance slices provide evidence for a second episode of karst formation at -1550 ms as the carbonate ramp started to aggrade (Figs. 20). These karsts develop above the most distal extent of the first karst episode, producing a branch pattern of apparent random orientation (Figs. 18a and 20). The aggrading platform subsequently shows a lack of karts or geometries diagnostic of sea-level fall for the rest of Unit 4, until the Late Miocene.

A final subaerial exposure event across 100-200 ms occurs beneath BB4 in the Late Miocene. Resulting karst forms are limited to the tops of the outer platform and the ICB to the NE (Figs. 14 and 16). Confined to a smaller area, the density of karst features is very high. The karsts are mainly circular depressions at start, and develop in patches. The karst network then becomes more branched and extends across the platform to the SE. The maximum density of karst features is reached at -1100 ms TWT. The branched karst network reduces in volume and retreats basinward at -1050 ms TWT, before being buried underneath the hemipelagites of Unit 5 (Fig. 16c).

## 6. Karst distribution

A density contour plot shows the greatest density of karsts to occur to the SE (Fig. 21a). This population of karsts overlies the inner ramp of the platform, with up to 140 karst features recorded within a 4 $km^2$ area (Fig. 21a). The cluster of karsts represents a first karstification event from -1700 to -1900 ms, which accounts for nearly 70% of all karsts observed across the study area (Fig. 21b).

Sparser populations of karsts occur in the NW and NE. These represent the third Late Miocene karstification event when only the platform margin and NW edges of the ICBs were exposed (Fig. 21a). Sub-aerial exposure at the end of the Miocene appears to have been short-lived when compared to the Early Miocene, with fewer than 5% of the karsts observed at this level. The densest Miocene karst, therefore comprises only 40 features within a 4 $km^2$ area (Fig. 21b).

Karst features exhibit statistical clustering across all horizons (Table 1). Results from the nearest neighbour ($R_n$) analysis show the first karst event in the Early Miocene to have the highest value at -1900 ms, with this value roughly halved by -1700 ms TWT i.e., showing the karst systems to have become more clustered over time. The second karst event at -1550 ms has the lowest $R_n$ ratio; therefore the Middle/Late Miocene karsts at the ramp margin are the most statistically clustered (Table 1). The third karst event also has a low $R_n$ ratio, showing the observed karst features to be clustered (Table 1).

## 7. Direct Hydrocarbon Indicators (DHIs)

There is multiple evidence for fluid migration in the study area. Migrating fluid is believed to comprise gaseous hydrocarbons sourced from underling faulted Jurassic strata. Based on the preserved morphology and seismic characteristics, fluid flow structures have been grouped into three families: 1) Vertical dim zones (VDZs), 2) gas pipes, and 3) pockmarks.

### *7.1 Vertical dim zones*

In the deeper successions, where pores are too tight to allow pipe formation, gases diffuse instead through the fracture matrix. Within Unit 4, the reflection continuity and amplitude is reduced beneath the platform margin. Vertical dim zones (VDZs), ranging in width from 50 m to 300 m, create zones of poor continuity without deforming the primary bedding (Fig. 12a). This change in seismic expression is interpreted to be the result of an irregular distribution of gas in the sediment, creating a low velocity zone which deteriorates the seismic data.

Vertical dim zones passing through the Eocene prograding sequences express themselves in variance slices as circular high-variance features (Fig. 22a). These surface expressions roughly trace out the trend of the prograding clinoforms, suggesting the location of the gas in the platform to be affected by the geometry of the Eocene carbonate ramp (Fig. 22a). Vertical dim zones terminate beneath an impermeable high-amplitude peak reflector within Unit 4. At the platform edge, this impermeable horizon shows poor continuity and the amplitude dims as VDZs pass through it (Fig. 22a). Above the impermeable area of the reflector vertical dim zones reappear, indicating lateral migration of fluid.

Following the second episode of karst development, short lived VDZs appear within a 100 ms TWT thick interval of dim horizontal reflections (Fig. 12a). Gases migrating through the karst network are unable to pass through the overlying impermeable horizon, therefore they migrate laterally toward the platform margin. A laterally extensive dim zone occurs in a 300 ms interval beneath the platform top. This dim zone is interpreted to be gas filled - the aggradation of the platform margin has created elevated topography which buoyant gas pools within (Fig. 12a).

### *7.2 Gas pipes*

A large number of small-scale gas pipes are found within Unit 5, which comprises less compact hemipelagic strata inherently favourable to pipe formation (Fig. 22b). Localised amplitude anomalies, phase reversal and reflection push-downs associated with the pipes support the presence of gas pockets or cemented zones at depth (Fig. 22b). The fact that reflections are still continuous suggests the sediments have not been remobilised by fluid flow. Evidence for gas migration in these units suggests the fluid to have been at a high pressure to fracture their way through low-permeability muddy sequences.

Pipe diameters range from 20 m to 250 m and vertical dimensions range from 50 to 250 ms TWT (Fig. 22a). Pipe size appears to increase toward the main salt diapir that occurs in the study area.

The largest pipes breach the surface and deflect the reflections upwards in a cone shape typical of mud volcanoes. The smallest pipes formed away from the diapir have a concave downward structure and do not breach the surface. Some of the smaller pipes terminate beneath BB4 (BB5), others just beneath the seabed within a bright spot or beneath continuous high amplitude reflections (Fig. 22b).

### *7.3 Pockmarks*

Pockmarks occur at all depths within the hemipelagites in Unit 5, and above Miocene karst systems (Fig. 22b). They provide an indication of fluid seepage at the seafloor following episodes of sub-aerial exposure in the Miocene and throughout the Holocene. They occur above the rimmed platform top, Late Miocene build-ups, Miocene faults and karst systems on the inner Miocene shelf (Fig. 22b). On seismic data, pockmarks appear as minor depressions that are 5-25 ms deep, sometimes with a central dim zone (Fig. 22b). Their diameter varies from 60 m to 100 m; generally the wider the pockmark the greater the vertical offset. On variance slices, palaeosurface anomalies are circular to elliptical, as opposed to the dendritic inclined karsts. With a high variance ring and low-variance core, pockmarks are similar to sinkholes. However, sinkholes form directly above karstified horizons, whereas the pockmarks form only within finer grained successions.

Most of the pockmarks show no spatial relationship with feeder gas pipes (Fig. 22b). However, the small population of pockmarks above the Early Miocene exposure surface show some degree of vertical continuity with underlying gas-filled sinkholes (Fig. 22b). A small number of domed features with dim zones are also observed in the Pliocene/Quaternary horizons. Explanations for these geometries include bioherms initiated within old pockmark sites, or pull-up effects owing to cemented high-velocity sediments.

## 8. Spatial analysis of DHIs

The spatial organisation of fluid flow features (sinkholes, vertical dim zones, gas pipes and pockmarks), have been grouped for analysis in Figure 23. Overall, fluids migrate from the inner ramp to ICBs in the Early Miocene, with the greatest concentration around the diapir and platform margin (Fig. 23a). A smaller population near to the surface clusters above Miocene faults (Fig. 23a).

The density of fluid-flow features ranges from zero to 350 pipes per 5 km². They are distributed in a clustered and uneven pattern across the area (Fig. 23a). A density plot shows the greatest density to occur in the NW (Fig. 23a). This area is situated above the Miocene platform top, on the NE flank of the salt diapir, with up to 410 DHIs recorded within 5 km² (Fig. 23a).

Another fluid flow cluster occurs on the SW flank of the diapir with 350 features per 5 km² (Fig. 23a). Both clusters correlate with a peak in fluid flow expression at -1150 ms TWT, where 17.5 % of all features are observed above karstified build-up surfaces. A third cluster of 190 features per 5 km² area overlies the ICB in the NE from the Late Miocene where lots of sinkholes were observed (Fig. 23a). In the proximal area there is no dense cluster of fluid-flow features, demonstrating a more scattered expression of DHIs across the shelf. Some 11.9% of all features were observed at -1700 ms, a depth that corresponds to the widespread fluid-flow features expressed as sinkholes and vertical dim spots above the first karstification event (Fig. 22b).

DHIs also occur through the distal ICBs in the NE, but are scarcer in the more proximal ICBs located to the SW. The small cluster in the East of the proximal setting overlies Miocene faults. There are no fluid flow features recorded beyond the platform margin in the NW; gas migration appears to have concentrated at the platform top and above distal ICBs by the Quaternary (Fig. 23a).

Fluid migration exhibits a statistical clustering across all mapped horizons (Table 2). The nearest neighbour ($R_n$) data show the fluid features at -650 ms TWT to have the lowest value. Therefore, fluid flow was most clustered in the Pliocene/Quaternary, as confirmed on seismic data by gas pipes breaching the seafloor on the flanks of the diapir (Fig. 23c). The values are only slightly greater for -950 ms and -1150 ms showing fluid migration to be also clustered in the Late Miocene. The $R_n$ value approaches 1 for the -1750 ms time-slice. At this depth, sinkholes interpreted to be gas filled are extensive on the ramp top, with vertical dim zones also occurring through the prograding clinoforms. This created a relatively widespread area over which gas migration is occurring at present.

## 9. Discussion

### *9.1 Oceanographic and tectonic controls on carbonate platform geometry*

The evolution of the Browse Basin from a carbonate ramp to a rimmed platform has previously been linked to enhanced nutrient-rich circulation in the Middle Miocene due to movement of the ITF across the narrowing Timor Sea (Rosleff-Soerensen et al., 2012). However, the 3D seismic data used in this study provides no evidence for major changes in ocean circulation during the Early to Middle Miocene start-up and keep-up phases of carbonate growth. Instead, increasing reef productivity in the Browse Basin during the Middle Miocene can be accounted for by a relative sea-level lowstand, when compared with the marked regional subsidence recorded in NW Australia above the Middle/Late Miocene boundary (Rosleff-Soerensen et al., 2016). The fact that carbonates in the Caernarvon Basin, to the south of the study area, failed to evolve from the ramp to the rimmed platform phase after the Middle Miocene (Rosleff-Soerensen et al., 2012) suggests that other factors, local to the Browse Basin, accounted for the high productivity evidenced by the thickly stacked reflections in Units 1 and 4 (Fig. 5).

Normal faulting as been suggested as a key controlling factor on carbonate growth offshore NW Australia (Saqab and Bourget, 2015; Courgeon et al., 2016; Rosleff-Soerensen et al., 2016) faults in the East of the study area are interpreted to relate to the collision of the Australian Plate with the

Banda Arc in the late part of the Early Miocene. In this same event, the outer shelf of the Miocene basin subsided as collision with SE Asia progressed (Stephenson and Cadman, 1994). Consequent to the fault initiation in the study area, the carbonate ramp evolved into a rimmed platform. With subsidence occurring on the hanging-wall fault blocks, there would have been reciprocal uplift on the corresponding footwalls. The offset would have enhanced a sea-level lowstand, and may have transferred the majority of the study area into shallow photic depths suitable for reef growth.

It should be noted, however, that there is no evidence in the interpreted data for ICB initiation or distribution to be directly controlled by underlying faults. Fault offsets are moderate throughout the Miocene, and ICBs are markedly absent from the faulted area to the east (Figs. 13 and 14). The ICBs in the study area are topographically restricted in their location, none developing beyond the NW extent of the Eocene ramp or Miocene platform margin, as also suggested (on a large-scale of analysis) by Rosleff-Soerensen et al. (2016) for the entire Northwest Shelf. This observation infers the NW part of the study area, beyond the interpreted carbonate build-ups, to be deeper than the photic zone (Fig. 13a).

During the Late Miocene i.e., towards Unit 5, the morphology of the ICBs reveals the impact of wind and wave activity on carbonate productivity and sedimentation (Schlager, 2005). Previous studies of ICBs in the Browse Basin found no evidence for strong surface currents to have had an impact upon carbonate development (Rosleff-Soerensen et al., 2012). However, Late Miocene build-ups (-1020 to -1360 ms deep) are seen to elongate perpendicular to the strike of the platform margin. A debris apron develops on the SE end of the build-ups, whilst the high-amplitude areas at the NW end suggests stronger growth or cementation (Figs. 16 and 17). The ICBs developed an asymmetrical cross-section defining a steeper windward side and a gentler leeward side, suggesting strong unidirectional wind and wave patterns (Schlager, 2005) (Fig. 16c). Changes in orientation and size of the build-ups may provide a new opportunity for reconstructing changes in wind pattern up to platform demise in the Browse Basin.

In the study area, the strengthening and rotation of wind and wave energy is found to coincide with the demise of carbonates in the outer Browse Basin. Changes in wind and wave patterns occur at a time of rapid subsidence in association with the deepening of the Timor Trough (O'Brien et al., 2002). Hence, in order to explain the development of the carbonate platform in the Middle Miocene, we propose that a combination of tectonic shallowing and flow of warmer tropical waters controlled the change from a carbonate ramp to a rimmed platform. In parallel, evidence in the 3D seismic dataset and hint at changing circulation patterns during the Late Miocene as being responsible for a subsequent reduction in carbonate production rates. In contrast to the Caernarvon Basin to the south, which failed to evolve from the carbonate ramp to the rimmed platform phase during the Late Miocene (Rosleff-Soerensen et al., 2012), ICBs developed in the Browse Basin because: a) the basin is located in near proximity to the temporal tropical transition b) the more northerly location of the outer Browse Basin was greatly controlled by nutrient input from the ITF and therefore, was more significantly affected by changes in its course, and c) the Browse Basin is nearer to the subduction zone and so there is greater associated faulting and uplift on the shelf top.

We propose the gradual drowning of the rimmed platform (and associated build-ups) at the end of the Miocene to result from decline in carbonate production rates due to unfavourable conditions in the basin caused by the formation of the Timor Trough. In such a setting, the decline in production rates may have occurred in response to similar conditions to those recorded offshore the Maldives, Indian Ocean. Here, a prominent turnover was recorded at the end of the Middle Miocene from a sea-level to a bottom current-controlled depo-environment (see Ludmann et al., 2013 and Rebesco et al., 2014 for comprehensive reviews). Drift units were therefore deposited within a large central basin enclosed by two chains of atolls. The partial drowning of the carbonated platform created connections to the Indian Ocean and established a complex current regime, with material shedding from the neritic platforms hindering their progradation (Lüdmann et al., 2013). Thus, in contrast to Roesleff-Soerensen (2012) we consider that nutrient upwelling and vigorous currents from Late Miocene have caused a dramatic change from aggradation to backstepping in ICBs of the

Browse Basin, following a drowning pattern usually attributed to episodes of rising sea level. This change denotes a pattern similar to that also recorded in the Maldives during the Late Miocene (Lüdmann et al., 2013).

The Late Miocene records a change in climatic conditions in the Browse Basin, from warm and wet to arid (McGowran and Li, 1996). In conjunction with the changes to regional climate, subduction was interpreted to have concentrated warm nutrient rich waters, which previously flooded the Northwest Shelf, into the deepening Timor Trough, thus leading to the demise of ICBs in the study area (O'Brien et al., 2002). In our model, the flow of nutrient rich ITF waters in the study area was capable of drowning the interpreted ICBs, in similarity to what is recorded in the Maldives. This phenomenon is perhaps better demonstrated on seismic data by the onset of sediment drift deposition downslope from the rimmed platform, and at a time when drowning occurred throughout the Browse Basin (Figs. 5 and 8c). Carbonate production continued in the Bonaparte Basin, likely due to the funnelling of ITF along the deeper part of the Timor Trough, away from shallow platform areas. In addition, the Bonaparte Basin is less exposed to incoming wind and waves of large fetch from the Indian Ocean creating an environment more favourable to carbonate growth after the Late Miocene.

### *9.2 Fluid flow paths and their economic and environmental significance*

The detection and evaluation of gas migration through the carbonate strata into impermeable to semi-impermeable Pliocene/Quaternary strata is critical to assess the petroleum potential of a sedimentary basin (Cartwright et al., 2007; Moss and Cartwright, 2010). The study of the inferred fluid pathways using the 3D seismic cube reduces exploration uncertainty relating to reservoir location, overpressure development and top seal capacity. Hence, the increasingly clustered organisation of fluid flow observed in the Browse Basin towards the Late Miocene suggests gas to have focused within the larger carbonate build-ups (Fig. 23a and Table 2). These ICBs are readily identifiable in the 3D seismic data and are usually considered key exploration targets for economic carbonate reservoirs (Wilson and Hall, 2010). Well documented analogues of carbonate sequences in hydrocarbon-rich areas include outcrops in Texas (Frost et al., 2012; Budd et al., 2013), in the Alps and Mediterranean regions (Antonellini et al., 2014; Jacquemyn et al., 2014; Whitaker et al., 2014), Miocene successions in SE Spain (Li et al., 2015) and vast carbonate units in the Middle East (Ehrenberg et al., 2012; Agada et al., 2014). In these analogue regions, the recognition of hypogenic and epigenic karsts is known to enhance porosity and diagenetic-related processes in otherwise homogeneous carbonate successions (Khalaf and Abdullah, 2013; Qi et al., 2014; Zhao et al., 2014).

Pockmarks, gas pipes and vertical dim zones are observed in the 3D seismic volume. Their presence provides evidence on the direction of general fluid flow and for overpressured strata nearby to an active, breached petroleum field (Hovland and Judd, 1988; Osborne and Swarbrick, 1997; Rogers et al., 2006; Betzler et al., 2011). The inferred fluid migration through the interpreted geological successions is intermittent in organisation and expression, yet persistent through time. In addition, clustering of DHIs suggests underlying structures focus fluid migration more efficiently than simple diffusive seepage through the sedimentary column (Gay et al., 2007). In the Eocene Unit 3, where fluid flow is first mapped as vertical dim zones, much of the gas clusters occur in prograding ramp-front strata. The relatively fine sediment deposited basinwards, and the progressive tilting of strata on the continental slope due to thermal relaxation and development of the Timor Trough, created fluid pathways for buoyant gases to pass through the shelf-edge/upper slope clinoforms (Cathro and Austin, 2001). As the Eocene ramp prograded >20 km, a large area was generated across the margin in which gas was (and is at present) migrating on its way to the surface (Fig. 23). A similar phenomenon is observed on the shallower Yampi Shelf, where large scale hydrocarbon seepage increases basinward due to progressive top-seal capillary failure (O'Brien et al., 2005).

A general spatial relationship is observed whereby fluid flow features are recorded to form clusters above underlying clusters of karst features (Fig. 24). This pattern demonstrates a systematic restriction of the majority of fluid migration to areas of enhanced permeability, which are the result of sea-level fall and local karstification (Loucks, 1999; Jiang et al., 2013) (see Fig. 7b). Widespread growth of the Browse Basin carbonate ramp began in the Early Miocene at the top of Unit 3. A relative sea-level fall superimposed karst systems and subsequent sinkholes onto the stratigraphy. Fluid migration is greatest and statistically least clustered at this interval (Figs. 24 and 25). The rapidly evolving ramp provides a broad, less predictable area over which fluid escapes from the Jurassic reservoir.

In the Middle Miocene, the majority of carbonate production relocated basinwards. High production rates at the platform margin (attributed to shallow warm waters) created a gentle topographic gradient. The presence of a salt diapir in the study area will have added to the focusing of fluid flow (Fig. 25). Hovland et al. (2015) propose that the accumulation, deformation, and transportation of salts may have several drivers and origins, including a process closely associated with hydrothermal activity. They defend that anhydrite and halite are due to evaporation of seawater with an unknown proportion being added by hydrothermal brines (Warren, 1999). Molecular theory, their own and past experiments, and reservoir modelling were used by Hovland et al. (2005) and Hovland et al. (2006a-c) to introduce the important new concept that, in some conditions, supercritical brines may deposit some of the salt deposits commonly interpreted as of 'geological' scales. Regardless of the origin of the salt forming the observed diapir, the flanks of salt structures are known areas of focused fluid migration - further enhanced in the study area by underlying karstification (and growth) of a large rimmed platform (Figs. 12a and 25). The salt diapir is therefore consider as the principal 'channel' for fluid flowing from deeper thermogenic sources in the Browse Basin. In addition, where thick and elevated carbonate bodies are buried adjacently to more compact lagoonal and basinal sediments, further landwards on the continental shelf, a lateral pore-fluid pressure gradient is established (Frazer, 2014). The ratio of permeability in the lateral and vertical migration paths exceeded the ratio of their lengths, encouraging gas flow away from the Early Miocene ramp top towards the Middle Miocene platform margin (Frazer, 2014). The main clusters of fluid flow occur above the more distal karst systems. There is no distinct population of fluid flow features in the Middle Miocene above the Eocene/Early Miocene inner-shelf karsts; fluids have been interpreted to flow laterally along reflections at various intervals. Therefore, vertical stacking of permeable zones (i.e. karst horizons and ramp margins) is not critical to the concentration of fluids.

Elevated mound geometry in Unit 4 ICBs (effective trap conditions) and surrounding lagoonal facies and overlying hemipelagics of Unit 5 (effective seal conditions) integrate several favourable elements of a petroleum system into one place (Burgess et al., 2013). However, the evidence of fluid flow above the ICBs indicates the seal capacity to have been breached by fluid under high pressures. Fluid flow above the build-ups in the NE and SW of the study area is of small scale and does not breach the surface (Fig. 25). This would suggest either a) seal capacity of the hemipelagites in Unit 5 is sufficient for trapping the gas, or b) concentration of gas is insufficient to create a pore fluid pressure to overcome the seal capacity of the hemipelagics (Osborne and Swarbrick, 1997). Considering the observed lateral migration of large amounts of fluid towards the platform margin, we believe scenario b) above to be the main cause for the minimal fluid seepage above the ICBs. This advocates irrelevant gas reserves within the ICBs, but fluid flow can be linked from deeper strata through the largest carbonate build-ups to the surface. Smaller build-ups which showing connection in the seismic to gas migration form unsuitable reservoirs for fluid sourced from below the carbonate platform (Fig. 25).

## 10. Conclusions

3D seismic data and borehole stratigraphic and wireline data allowed the investigation into the evolution of the outer Browse Basin. The effect stratigraphy has on fluid flow and the ramifications this has upon the reservoir potential and environment of the basin have been discussed. Main findings in this work include:

1) Initiation of ramp phase carbonate growth during the Early Miocene took place above the palaeotopography of the Eocene ramp. Seismic geometries during Middle Miocene suggest evolution to the platform phase resulted from tectonic activity (i.e. collision of Australia with the Banda Arc) which created a shallow environment and transported the Browse Basin into tropical waters inducive to reef growth.

2) The location of isolated carbonate build-ups (ICBs) appears unrelated to fault topography, they are merely limited to the extensive shallow environment created by the Miocene platform. However, seismic evidence of ICB debris deposits during the Late Miocene records more than 45° rotation in incoming wind and wave direction. Concentration of wave energy at the steep reef edge topography as sea level fell, significantly weakened the health of carbonate growth prior to subaerial exposure followed by drowning at the end of the Miocene

3) Late Miocene tectonics also diverted into the study area. This study proposes the introduction of a strong ITF to be associated with the demise of carbonate systems in the Browse Basin, on account of its impact upon the palaeoceanographic regime and nutrient supply to the Northwest Shelf.

4) Clustered vertical dim zones and sinkholes above Miocene karst systems demonstrates sea level fall to enhance strata permeability, causing fluid migration across the extent of the exposure surface.

5) Within the carbonate topography of the Middle and Late Miocene, fluid migrates along pressure gradients from basinal and lagoonal settings updip into the platform margin and the larger ICBs. Finer grained lagoonal and basinal sediments, and overlying Pliocene/Quaternary hemipelagics commonly form suitable seal intervals to hydrocarbon plays.

6) The dataset shows that, apart from a shelf-edge diapir, Miocene ICBs are the focus for fluid migration in the Browse Basin. Samples taken from Poseidon-1 and Poseidon-2 will either support or disclaim the significance of methane on carbonate growth. Yet, the presence of deep reservoir intervals in syn-rift strata of the Browse Basin, and the evidence for fluid flow below -1700 ms TWT depth, indicates that the source of fluid is located below the studied carbonate successions. Findings herein could assist the discovery of deep reservoir intervals elsewhere in the Timor Sea, and on Equatorial Margins as a whole.

## Acknowledgements

We acknowledge the support of Geosciences Australia in this work. We thank C. Kirkham (Cardiff) for help provided with the $R_n$ tests on ESRI software. Also thanked are the editor-in-chief M. Rebesco and reviewers M. Hovland and Ch. Hübscher, who provided constructive comments to this work. T. Alves dedicates this paper to the memory of Prof. J. Pais, who introduced the importance of the Miocene period to the author, back in the 1990s. Long gone, but not forgotten, are his exquisite explanations about marine depositional environments, foraminifera and, I dare say, shark teeth, in the balmy Tagus Basin.

## REFERENCES

Agada, S., Chen, F., Geiger, S., Toigulova, G., Agar, S., Shekhar, R., Benson, G., Hehmeyer, O., Amour, F., Mutti, M., Christ, N., Immenhauser, A., 2014. Numerical simulation of fluid-flow processes in a 3D high-resolution carbonate reservoir analogue. Petrol. Geosc. 20, 125-142.

AGSO North West Shelf Study Group. 1994. Deep reflections on the North West Shelf: changing perceptions of basin formation. In The Sedimentary Basins of Western Australia: Proceedings of the Western Australian Basins Symposium, Perth, WA, PESA, pp. 63-76.

Ahr W.M. 1973. The carbonate ramp: an alternative to the shelf model. Trans. Gulf Coast Association of Geol. Soc., 23rd Annu. Conv. 221-225.

Antonellini, M., Cilona, A., Tondi, E., Zabrano, M., Agosta, F., 2014. Fluid flow numerical experiments of faulted porous carbonates, Northwest Sicily (Italy). Mar. Petrol. Geo. 55, 186-201.

Apthorpe M. 1988. Cainozoic depositional history of the North West Shelf. In: Purcell, P.G., Purcell, R.R. (Eds.), The North West Shelf, Australia. Proceedings of Petroleum Exploration Society of Western Australia Symposium, Perth.55-84.

Betzler, C., Fürstenau, J., Lüdmann, T., Hübscher, C., Lindhorst, S., Paul, A., Reijmer, J., Droxler, A., 2013. Sea-level and ocean-current control on carbonate-platform growth, Maldives, Indian Ocean. Basin Res. 25(2), 172-196.

Betzler, C., Hübscher, C., Lindhorts, S., Reijmer, J., Römer, M., Droxler, A., Fürstenau, J., Lüdmann, T., 2009. Monsoonal-induced partial carbonate platform drowning (Maldives, Indian Ocean). Geology, 37(10), 867 - 870.

Betzler C., Lindhorst S., Hübscher C., Lüdmann T., Fürstenau J. and Reijmer J. 2011. Giant Pockmarks in a carbonate platform (Maldives, Indian Ocean). Mar. Geol. 289, 1-16.

Bosence D. 2005. A genetic classification of carbonate platforms based on their basinal and tectonic settings in the Cenozoic. Sed. Geol. 175, 49-72.

Bradshaw M.T., Bradshaw J., Murray A., Needham J., Spencer L., Summons R.E., Wilmot J. and Winn S. 1994. Petroleum systems in West Australian basins. P.G. Purcell, R.R. Purcell (Eds.). The Sedimentary Basins of Western Australia: Proceedings of the Petroleum Exploration Society of Australia. Perth, 1994, pp. 93–118

Brown A. 2000. Evaluation of possible gas microseepage mechanisms. AAPG Bull. 84, 1775–1789

Brown, A.R., 2004. Interpretation of Three-dimensional Seismic Data, sixth ed. American Association of Petroleum Geologists, Tulsa.

Budd, D.A., Frost, E.L., Hunttington, K.W., Allwardt, P.F., 2013. Syndepositional deformation features in high-relief carbonate platforms: long-lived conduits for diagenetic fluids. J. Sed. Res. 83, 12-36.

Burgess P. M., Winefield P., Minzoni M., and Elders C. 2013. Methods for identification of isolated carbonate buildups from seismic reflection data: AAPG Bull. 97, no.7, p. 1071-1098.

Cartwright J. (2007). The impact of 3D seismic data on the understanding of compaction, fluid flow and diagenesis in sedimentary basins. J. Geol. Soc., London 164(5), 881-893.

Cathro D.L. and Austin J.A. 2001. An early mid-Miocene, strike parallel shelfal trough and possible karstification in the Northern Carnarvon Basin, North West shelf, Australia. Mar. Geol. 178, 157-169.

Collins L.B. 2010. Controls on Morphology and Growth History of Coral Reefs of

ConocoPhillips. 2010. Poseidon-1 and Poseidon-2 Well Completion Reports, Volume-1: Basic Data. ConocoPhillips (Browse Basin) Pty Ltd.

Courgeon, S., Bourget, J. and Jorry, S.J. 2016. A Pliocene-Quaternary analogue for ancient epeiric carbonate settings: The Malita intrashelf basin (Bonaparte basin, northwest Australia). AAPG Bull. 100, 565-595.

Ding X, Bassinot F., Guichard F., & Fang N. Q. 2013. Indonesian Throughflow and monsoon activity records in the Timor Sea since the last glacial maximum. Mar. Micropal. 101 (0), 115-126.

Eberli G.P., Masaferro J.L. and Sarg J.F. 2004 Seismic imaging of carbonate reservoirs and systems, in Seismic imaging of carbonate reservoirs and systems. AAPG Memoir 81, 1-9.

Ehrenberg, S.N., Walderhaug, O., Bjorlykke, K., 2012. Carbonate porosity creation by mesogenetic dissolution: Reality or illusion? AAPG Bull. 96, 217-233.

Fournillon A., Abelard S., Viseur S., Arfib B. and Borgomano J. 2012. Characterisation of karstic networks by automatic extraction of geometrical and topological parameters: comparison between observations and stochastic simulations. Geol. Soc., London, Sp. Pubs. 370 (1), 247-264.

Frost, E.L., Budd, D.A., Kerans, Ch., 2012. Syndepositional Deformation in a high-relief carbonate platform and its effect on early fluid flow as revealed by dolomite patterns. J. Sed. Res. 82, 913-932.

Gallagher S.J., Wallace M.W., Li C.L., Kinna B., Bye J.T., Akimoto K. and Torii M. 2009. Neogene history of the West Pacific Warm Pool, Kuroshio and Leeuwin currents. Palaeoceanography 24, doi:10.1029/2008PA001660.

Gay A., Lopez M., Berdt C. and Séranne M. 2007. Geological controls on focused fluid flow associated with seafloor seeps in the Lower Congo Basin. Mar. Geol. 244, 1-4, 68-92.

Ginsburg R.N. and James N.P. 1974. Holocene carbonate sediments of continental shelves. In: C.A. Burke and C.L. Drake (Editors), The Geology of Continental Margins, Springer-Verlag, New York, N.Y., 137-155.

Haq B., Hardenbol J. and Vail P. 1987. Chronology of fluctuating sea-levels since the Triassic. Science 235, 1156-1167.

Harrowfield M. and Keep M. 2005. Tectonic modification of the Australian North-West Shelf: episodic rejuvenation of long-lived basin divisions. Basin Res. 17(2), 225-239.

Hart B.S. 1999. Definition of subsurface stratigraphy, structure and rock properties from 3-D seismic data. Earth-Sci. Reviews 47, 189-218.

Heyward A. A., Pinceratto E. E. and Smith L. L. 1997. Big Bank Shoals of the Timor Sea: an environmental resource atlas, Australian Institute of Marine Science & BHP Petroleum.

Ho S., Cartwright J.A. and Imbert P. 2012. Vertical evolution of fluid venting structures in relation to gas flux, in the Neogene-Quaternary of the Lower Congo Basin, Offshore Angola. Mar. Geol. 332-334, 40-55.

Holloway P. E., Chatwin P.G. and Craig P. 2001. Internal tide observations from the Australian North West Shelf in summer 1995. J. Phys. Oceanogr. 31(5), 1182–1199

Holloway P.E. and Nye H.C. 1985. Leeuwin current and wind distributions on the southern part of the Australian North West Shelf between January 1982 and July 1983. Australian J. Mar. Fresh. Res. 36 (2), 123-137.

Hovland, M. 1985. Carbonate cemented pillars at Nesøya, North Norway: Proposal for an alternative model of formation. Norsk Geo. Tidss. 65, 221-223.

Hovland, M. and Judd, A.G., 1988. Seabed Pockmarks and Seepages. Impact on Geology, Biology and the Marine Environment. Graham and Trotman Ltd., London, 293.

Hovland, M., Croker, P.F. and Martin, M. 1994. Fault-associated seabed mounds (carbonate knolls?) off western Ireland and north-west Australia. Mar. Petr. Geol. 11, 232-246.

Hovland, M. 2008. Hydrothermal salt – but how much? Mar. Petr. Geol. 25, 191-202.

Hovland, M., Rueslåtten, H. and Johnsen, H.K. 2015. Red Sea salt formations – A result of hydrothermal processes. *In:* Rasul, N.M.A and Stewart, I.C.F. (Eds.), The Red Sea. Springer-Verlag Sciences, pp. 187-203.

Jacquemyn, C., El Desouky, H, Hunt, D., Casini, G., Swennen, R., 2014. Dolomitization of the Latemar platform: Fluid flow and dolomite evolution. Mar. Petr. Geol. 55, 43-67.

John C.M., Karner G.D. and Mutti M. 2004. $\delta^{18}O$ and Marion plateau backstripping: combining two approaches to constrain late middle Miocene eustatic amplitude. Geology 32, 829–832.

Keall J.M and Smith P.J. 2004. The Argus-1 gas discovery, northern Browse basin, Australia. *In:* G.K. Ellis, P.W. Baillie, T.J. Munson (Eds.), Timor Sea Petroleum Geoscience. Proceedings of the Timor Sea Symposium, Darwin, 19–20 June 2003, Northern Territory Geological Survey, Special Publication 2004 1, 38–52.

Khalaf, F.I. and Abdullah, F.A. 2013. Petrography and diagenesis of cavity-fill dolocretes, Kuwait. Geoderma 207-208, 58-65.

Langhi L. and Borel G.D. 2007, Reverse structures in accommodation zone and early compartmentalisation of extension system, Laminaria High (NW shelf, Australia). Mar. Petr. Geol. 25, 791-803.

Lees B.G. 1992. Recent terrigenous sedimentation in Joseph Bonaparte Gulf, Northwestern Australia. Mar. Geol. 103, 199-213.

Li, Z., Goldstein, R.H., Franseen, E.K., 2014. Geochemical record of fluid flow and dolomitization of carbonate platforms: ascending freshwater–mesohaline mixing, Miocene of Spain. *In:* Agar, S.M. and Geiger, S. (eds). *Fundamental Controls on Fluid Flow in Carbonates: Current Workflows to Emerging Technologies*. Geol. Soc., London Sp. Pub. 406, 115-140.

Longley I.M., Buessenschuett C., Clydsdale L., Cubitt C.J., Davis R.C., Johnson M.K., Marshall N.M., Murray A.P., Somerville R., Spry T.B. and Thompson N.B. 2002. The North West Shelf of Australia- a Woodside perspective. P.G. Purcell, R.R. Purcell (Eds.), The Sedimentary Basins of Western Australia: Proceedings of the Petroleum Exploration Society of Australia 3. Perth, 2002, pp. 27-88

Løseth H., Gading M. and Wensaas L. 2009. Hydrocarbon leakage interpreted on seismic data. Mar. Petr. Geol. 26, 1304-1309.

Loucks R.G. 1999. Paleocave carbonate reservoirs: Origins, burial-depth modifications, spatial complexity and reservoir implications: AAPG Bull. 83, 1795-1834.

Lüdmann, T., Kalvelage, C., Betzler, C., Fürstenau, J., Hübscher, C., 2013. The Maldives, a giant isolated cabonate platform dominated by bottom currents. Mar. Petr. Geol. 43, 326-34.

Marfurt K.J. and Alves T.M. 2015. Pitfalls and limitations in seismic attribute interpretation of tectonic features. Interpretation 3, 1-11.

Marshall J., Davies P., Mihut I., Troedson A., Bergerson D. and Haddad D. 1994. Sahul shoals processes: Neotectonics and Cainozoic environments-cruise 122: Post Cruise Report. Australian Geological Survey Organisation, Canberra.

McGowran, B., Holdgate, G.R., Li, Q. and Gallagher, S.J., 2004. Cenozoic stratigraphic succession in southeastern Australia. Austral. J. Earth Sci. 51, 459-496.

Mcgowran B. and Li Q. 1996. Ecostratigraphy and sequence biostratigraphy, with a neritic foraminiferal example from the Miocene in southern Australia. J. Hist. Biol. 11, 136-169.

Mitchell A. 2005. The ESRI guide to GIS analysis. Volume 2: Spatial measurements and statistics: California, ESRI Press, 238p.

Moss J.L. and Cartwright J. 2010. 3D seismic expression of km-scale fluid escape pipes from offshore Namibia. Basin Res. 22. 481–501. doi: 10.1111/j.1365-2117.2010.00461.x

Nicholas W.A., Nichol S.L., Howard F.J.F. Howard, Picard K., Dulfer H., Radke L.C., Carroll A.G., Tran M. and Siwabessy P.J.W. 2014. Pockmark development in the Petrel Sub-basin, Timor Sea, Northern Australia: Seabed habitat mapping in support of CO2 storage assessments. Cont. Shelf Res. 83, 129-142.

O'Brien G. W., Glenn K., Lawrence G., Williams A. K., Webster M., Burns S. and Cowley R. 2002. Influence of hydrocarbon migration and seepage on benthic communities in the Timor Sea, Australia. APPEA journal.

O’Brien G.W., Lawrence G.M., Williams A.K., Glenn K., Barrett A.G., Lech M., Edwards D.S., Cowley R., Boreham C.J. and Summons R.E. 2005. Yampi Shelf, Browse Basin, North-West Shelf, Australia: a test-bed for constraining hydrocarbon migration and seepage rates using combinations of 2D and 3D seismic data and multiple, independent remote sensing technologies. Mar. Petrol. Geol. 22, 517-549.

Omosanya K.O. and Alves T.M. 2013. A 3-dimensional seismic method to assess the provenance of Mass-Transport Deposits (MTDs) on salt-rich continental slopes (Espírito Santo Basin, SE Brazil). Mar. Geol. 44, 223-239.

Osborne M.J. and Swarbrick R.E. 1997. Mechanisms for generating overpressure in Sedimentary Basins: A Re-evaluation. AAPG Bull. 81(6), 1023-1041.

Peel M.C., Finlayson B. L. and McMahon T. A. 2007. Updated world map of the Köppen-Geiger climate classification. Hydr. Earth Syst. Sci. Disc. 4(2), 439-473.

Powell D.E. 1976. The geological evolution of the continental margin off northwest Australia. APEA journal, 16(1) 13-23.

Prinzhofer, A. and Deville, E. 2013. Origins of hydrocarbon gas seeping out from offshore mud volcanoes in the Nile delta. Tectonophysics 591, 52-61.

Qi, J., Zhou, H. and Marfurt, K. 2014. Attribute expression of fault-controlled karst — Fort Worth Basin, Texas: A tutorial. Interpretation 2, SF91-SF110.

Rayson M.D., Ivey G.N., Jones N.L., Meuleners M.J. and Wake G.W. 2011. Internal tide dynamics in a topographically complex region: Browse Basin, Australian North West Shelf. J. Geophys. Res., Oceans (1978-2012), 116 (C1).

Read, J.F., 1985. Carbonate platform facies models. AAPG Bull. 69, 1-21.

Rebesco, M., Hernández-Molina, F.J., van Rooij, D. and Wåhlin, A. 2014. Contourites and associated sediments controlled by deep-water circulation processes: State-of-the-art and future considerations. Mar. Geol. 352, 111-154.

Rogers J.N., Kelley J.T., Belknap D.F., Gontz A. and Barnhardt W.A. 2006. Shallow–water pockmark formation in temperate estuaries: a consideration of origins in the western gulf of Maine with special focus on Belfast Bay. Mar. Geol. 225, 45–62.

Rosleff-Soerensen B., Reuning L., Back S. and Kukla P. 2012. Seismic geomorphology and growth architecture of a Miocene barrier reef, Browse Basin, NW-Australia. Mar. Petrol. Geol. 29, 233-254.

Rosleff-Soerensen B., Reuning L., Back S. and Kukla P. 2016. The response of a basin-scale Miocene barrier reef system to long-term, strong subsidence on a passive continental margin, Barcoo Sub-basin, Australian North West Shelf. Basin Res. 28, 103-123.

Saqab M. M. and Bourget J. 2015. Controls on the distribution and growth of isolated carbonate build-ups in the Timor Sea (NW Australia) during the quaternary. Mar. Petr. Geol. 62, 123-143

Schlager W. 2005. Carbonate sedimentology and sequence stratigraphy (No. 8). SEPM, Spec. Pubs. 200 pp.

Serié, C., Huuse, M. and Schødt, N.H. 2012. Gas hydrate pingoes: Deep seafloor evidence of focused fluid flow on continental margins. Geology 40, 207-210.

Stephenson, A.E. and Cadman, S.J., 1994. Browse Basin, northwest Australia: the evolution, paleogeography and petroleum potential of a passive continental margin. Palaeog., Palaeoclim.y, Palaeoecol. 111, 337-366.

Testa, V. and Bosence, D.W.J. 1999. Physical and biological controls on the formation of carbonate and siliciclastic bedforms on the north-east Brazilian shelf. Sedimentology 46, 279-301.

Tovaglieri F. and George A.D. 2014. Stratigraphic architecture of an Early-Middle Jurassic tidally influenced deltaic system (Plover Formation), Browse Basin, Australian North West Shelf. Mar. Petr. Geol. 49, 59-83.

Van Gastel P., Ivey G.N., Meuleners M.J., Antenucci J.P. and Fringer O. 2009. The variability of the large-amplitude internal wave field on the Australian North West Shelf. Cont. Shelf Res. 29(11–12), 1373–1383

Veevers J.J. 1967. The Phanerozoic geological history of northwest Australia. J. Geol. Soc. Aust., 14 (2), 253-277.

Wenau, S., Spiess, V., Pape, T. and Fekete, N. 2015. Cold seeps at the salt front in the Lower Congo Basin II: The impact of spatial and temporal evolution of salt-tectonics on hydrocarbon seepage. Mar. Petrol. Geo. 67, 880-883.

Whitaker, F.F., Felce, G.P., Benson, G.S., Amour, F., Mutti, M. and Smart, P.L., 2014. Simulating flow through forward sediment model stratigraphies: insights into climatic control of reservoir quality in isolated carbonate platforms. Petrol. Geos. 20, 27-40.

Wilson, M.E.J. 2012. Equatorial carbonates: an earth systems approach. Sedimentology 59, 1-31.

Wilson, M.E.J. 2002. Cenozoic carbonates in Southeast Asia: implications for equatorial carbonate development. Sed. Geo. 147, 295-428.

Wilson, M.E. and Hall, R. 2010. Tectonic influences on SE Asian carbonate systems and their reservoir development: Cenozoic Carbonate Systems of Australasia: SEPM, Special Publication 95, 13-40.

Wu, L., Trudgill, B.D. and Kluth, C.F. 2016. Salt diapir reactivation and normal faulting in an oblique extensional system, Vulcan Sub-basin, NW Australia. J. Geol. Soc., London, doi:10.1144/jgs2016-008.

Zhao, W., Shen, A., Qiao, Z., Zheng, J. and Wang, X. 2014. Carbonate karst reservoirs of the Tarim Basin, northwest China: Types, features, origins, and implications for hydrocarbon exploration. Interpretation 2, SF65-SF90.

**Figure Captions**

**Figure 1** – (a) General map of Australia highlighting the location of the Browse Basin in the greater North West Shelf, Australia. (b) Tectonic elements map of the North West shelf of Australia showing the various basins and sub-basins, hydrocarbon discoveries and the location of the study area. Modified from Bernecker (2011). (c) Simplified bathymetric map of the Browse Basin showing its main structural elements. The region analysed by Rosleff-Soerensen et al. (2012) is located to the SW of the study area. Major Palaeozoic faults strike NE-SW throughout the study area (see Harrowfield and Keep, 2005). The profile A-A’ is shown in Figure 2.

**Figure 2 -** Interpreted seismic section A-A’ across the central part of the Browse Basin, imaging the Yampi Shelf and the Caswell Sub-Basin (Geoscience Australia, 2013; Ding et al., 2013; Australian Government Department of Industry Geoscience Australia, 2014). See Figure 1c for location of the seismic section.

**Figure 3** - Stratigraphic chart of the Browse Basin area showing the names of significant hydrocarbon fields and associated tectonic events. The nomenclature of units and tectonic events is based on the Vulcan and Bonaparte basins. Oil (black), oil and gas (red) and gas (green) discoveries are noted on the chart. Modified from AGSO North West Shelf Study Group (1994) and ConocoPhillips (2010).

**Figure 4** - Normal distribution curve demonstrating the significance levels of critical values of the Z-score and how they relate to the spatial distribution of point data (from ESRI, 2013).

**Figure 5 –** NW-SE seismic profile highlighting the seven mapped horizons BB0, BB1, BB2, BB3, BB4, BB5 and BB6, and Units 1-5 as referred to in the text. Ages have been given constrained by tying the seismic data with Poseidon-1 and Poseidon-2 wells. See Fig. 6a for location of the seismic line.

**Figure 6 –** (a) Time-structural map of Horizon BBO showing incision of a tidal inset in the north of the study area. The remainder of the surface is relatively continuous, steepening towards the NW. (b) RMS amplitude map of BBO showing the low-amplitude nature of the channel incision surface and the very general decrease in seismic amplitude to the NW, owing to a finer more muddy units in the deeper distal setting. (c) NW-SE seismic section highlighting the presence of a salt diapir on the shelf-edge. There is no data available in this study from within the diapir. See Fig. 6a for location.

**Figure 7 –** (a) Surface oceanography of the present day Indo-Pacific region. Black arrows show warm currents and grey arrows show cold currents. The 200 m bathymetric contour, representing the shelf edge in the study area, is indicated. The small insert shows a close up of the ocean circulation through the study area (marked by a red arrow). See the west flowing South Java current

and the Indonesian Throughflow (ITF) sweeping through the Timor Sea (Gallagher et al., 2009). (b) Eustatic sea-level curve showing both short and long term variation since the Paleocene. Sea level can be seen to have gradually fallen over the past 60 Ma (from Haq et al., 1987). Cenozoic regional unconformities and major events in the Timor Sea are identified. They are chiefly associated with large-scale plate movements (adapted from Saqab and Bourget, 2015).

**Figure 8 –** (a) NE-SW seismic profile showing BB3 in a relatively proximal setting, where it divides chaotic karstified horizons above and below. The break in slope marks the boundary between the karstified proximal ramp and the more distal lower ramp. (b) NE-SW seismic profile showing the nature of BB3 in a distal setting where it separates prograding (but relatively continuous) seismic reflections of the lower ramp. A steep break in slope marks the edge of the ramp, where reflection continuity in BB3 is locally lost. (c) NW-SE seismic profile highlighting the seismic character of BB4 in a more distal setting. BB4 overlies chaotic facies and is onlapped by continuous reflections on top. Behind the break in slope, reflections are relatively flat, and slope very gently into the back-reef behind the platform. A mound marks the edge of the carbonate platform. The location of the seismic profiles is shown in Fig. 6.

**Figure 9** – (a) Variance slice at a depth of Z=-2352 ms TWT showing tidal inlets within Unit 2. The proximal region of the platform is smooth, with relative low variance when compared with the distally incised region. (b) NW-SE seismic profile highlighting that surfaces BB1 and BB2 define Unit 2. Seismic reflections in this unit start by forming progradational clinoforms, which define the early ramp stage. Clinoforms first advance >10 km basinward and, in asecond stage, develop a more aggradational nature. The clinoform tops are smooth and continuous. See Fig. 10a for the location of the seismic line.

**Figure 10 -** (b) NW-SE seismic profile showing characteristic reflection geometries in Unit 3. Four prograding wedges are outlined as T1-T4 in the figure, following the order in which they grew. The blue dashed line shows the Oligocene unconformity in the distal region, where toplap reflections indicate down-stepping and erosion. At the end of Unit 3, reflections onlap this latter unconformity. See Fig. 10a for the location of the seismic profile. (c) NW-SE seismic profile highlighting the geometry of internal reflections in Unit 3, in the proximal part of the Browse Basin. The blue dashed line shows the Oligocene surface over which strata appear conformable – probably indicating a sediment hiatus rather than a stratigraphic unconformity. This event marks the initiation of carbonate production on the ramp. See Fig. 10a for location of the seismic line.

**Figure 11 –** (a) Variance slice at a depth of -1920 ms TWT through Unit 3 showing dendritic karsts forming on the inner ramp, the area effected by karsts is outlined in yellow. The break in slope and the positioning of the advancing clinoforms are highlighted by NE-SW linear bands of high variance.

**Figure 12** - (a) NW-SE seismic profile showing the distal section of Unit 4. The dashed black line represents a shift from a carbonate ramp to a rimmed tropical platform. Arrows indicate the general direction of carbonate growth, from a basinwards direction (progradation) in the Early Miocene to upwards (aggradation) in the Middle-Late Miocene. (b) Seismic line showing the proximal section of Unit 4. Areas are labelled to highlight the changes in seismic facies observed on the platform top; Small mounds and karsts in horizontal beds to larger carbonate build ups without any karsts. The topmost reflections of Unit 4 onlap the Late Miocene build-up from the SE. See Fig. 13a for the location of the two seismic profiles in this figure.

**Figure 13 –** (a) RMS amplitude map of Unit 4 showing the highest amplitudes to occur on the NW margins of the build-ups and also in the distal incisions on the NW slope of the platform. Away

from the build-ups, amplitude decreases into the continental shelf, implying a decrease in grain size. (b) 3D organisation of evolving Isolated Carbonate Build-ups (ICBs) from -1750 to -1050 ms TWT. There are two main clusters of build-ups, one in the NE where rounded build-ups stack above one another, and a second in the SW - not as long lived but more laterally extensive. Smaller sub-circular build-ups developed in a scattered array across the remainder of the study area.

**Figure 14 -** Outline of areas with isolated carbonate production within the study area. The figures represent depths from -1750 to -1050 ms TWT (a-h), and highlight the 2D areas of ICBs. Grid squares in the figure are 4 $km^2$.

**Figure 15 -** Graph demonstrating the variation ICBs' area as outlined in Fig. 14. The data points are labelled with the calculated 2D areas of ICBs, in $km^2$. The area of ICBs increases from -1750 ms to -1250 ms TWT, subsequently declining and ending at a TWT depth of -950 ms.

**Figure 16** – RMS Amplitude maps of Unit 4 showing an ICB in the NE corner of the study area (refer to Fig. 14e for location). Arrows indicate the location of the steeper higher amplitude margin. a) Horizon BB4. b) RMS amplitude map within Unit 5. (c) Seismic line through the corresponding ICB in the NE. Note the seismic pull-up effect observed beneath the steeper NW margin. Figure 16b shows the location of the seismic line.

**Figure 17-** Graph highlighting changes in area of the debris apron in the NE ICB, from -1280 to -1020 ms TWT. The area of the debris apron increases sharply at -1240 ms TWT. It peaks at -1180 ms TWT, and subsequently falls before the carbonate build-up is drowned.

**Figure 18 –** (a) Seismic line and variance slice at Z=-1900 ms TWT showing the signature chaotic, circular depressions (occasionally with an anastomotic pattern) of karsts above the Oligocene

unconformity in Unit 3. See Fig. 19 for location of the seismic line. (b) Karsts (green spheres) mapped from -1900 to -1050 ms TWT. These are visualised in 3D with the BB2 and BB4 surfaces for reference. Note how the karsts evolve from the Eocene ramp top, out to the platform margin by the Late Miocene.

**Figure 19 -** Variance slice at Z=-1700 ms TWT showing a shift in karstified strata from the inner ramp to the break in slope. Insert shows the karst geometries to have formed a more branched to dendritic pattern than the karsts of the inner ramp in Fig. 20.

**Figure 20 -** Seismic profiles showing the three main karst episodes recorded in the seismic during the Miocene. The first karst system forms in the Early Miocene at the start of carbonate production and is laterally very extensive across the shelf top. Bright spots represent sinkholes and pockmarks forming above the karsts in the more continuous horizons. The second episode advanced basinwards of the first episode, following the shift of the carbonate factory into the basin as it enters the rim phase of growth. Above this karst system a high amplitude continuous reflection with occasional depressions is interpreted to represent pockmarks within a finer sediment, overlying horizontal reflections have a dimmed amplitude (see circles in inset). The third and final karst system concentrates at the platform margin in the Late Miocene, prior to the demise of the platform. The insets show these episodes in greater detail. See Fig. 18 for location.

**Figure 21** – (a) Contour plot for karst data showing areas of higher density in red. There are three visually clustered populations, the largest of which occurs on the inner ramp. Smaller populations are observed above the platform margin and ICBs. (b) Bar chart highlighting the frequency of Miocene karst features recorded at 100 ms TWT intervals. The graph shows the majority of karsts to have formed in the Early Miocene, from -1900 to -1600 ms TWT. A much smaller population of karsts developed between -1300 and -1000 ms TWT.

**Figure 22** – (a) Seismic line and translucent variance slice at Z=-1700 ms TWT showing sub-circular sinkholes above karstified strata of Oligocene/Early Miocene age. Inset shows some of these features to have a mounded form and an inner bright zone in seismic section. See Fig. 19 for location. (b) Seismic line showing thinner gas pipes forming away from the diapir above a Late Miocene exposure surface. All pipes have a concave-downward cross section, which translates to a circular time-slice expression. Some pipes terminate beneath the high-amplitude Horizon BB5. Two gas pipes close together in Unit 5 merge into one in Unit 6.

**Figure 23 –** (a) Density contour plot for the fluid flow features. The main populations occur in the distal setting above the platform margin and surrounding the salt diapir, as well as above the ICB in the NE. (b) Bar chart to show the frequency of fluid flow features from the Early Miocene to Pliocene/Quaternary, at 100 ms TWT intervals. The fluid flow features recorded include sinkholes, vertical dim spots, pipes and pockmarks. The graph demonstrates two clear peaks in the fluid flow expression, one at -1750 ms TWT following the first karstification event in the Oligocene, and a second at -1150 ms TWT following the third karstification event in the Late Miocene. There are far fewer fluid flow features recorded in the Pliocene/Quaternary.

**Figure 24 –** Density overlay of fluid-flow features and karsts showing a correlation between fluid-flow clusters and distal karst systems.

**Figure 25** - Schematic representation of the studied volume with a synthesis of fluid-flow concentration relative to the stratigraphy and local structures.

**Table 1 –** Statistical results of an average nearest-neighbour ratio test for the karst data at various intervals identified to be of stratigraphic importance in the evolution of the platform. The final row is the result for all karsts mapped.

**Table 2 -** Results of a nearest neighbour test for fluid-flow features between -650 and -1900 ms TWT. Results are given for certain time slices interpreted to be of stratigraphic significance, and

then for the entire dataset. Also shown are the nearest neighbour ratio, and z-score. The most statistically clustered horizon occurs at -650 ms TWT, just beneath the seafloor.

| Depth (TWT) | Platform environment | Nearest-Neighbour Ratio ($R_n$) | Z-score | Spatial Pattern |
|---|---|---|---|---|
| -1900 ms | Initiation of carbonate factory above Oligocene unconformity, base of 1st karstification event. | 0.824 | -11.095 | Clustered |
| -1700 ms | First karstification event extends to ramp edge. | 0.496 | -24.331 | Clustered |
| -1550 ms | Middle Miocene, platform begins to aggrade. Second karstification event. | 0.354 | -28.209 | Clustered |
| -1050 ms | Late Miocene. Third and final karstification event before the drowning of the carbonate system. | 0.472 | -10.604 | Clustered |
| -1050 to -1900 ms | Entire succession from initiation to demise of the carbonate factory. | 0.738 | -35.481 | Clustered |

Table 1

| Depth (TWT) | Stratigraphic Significance | Nearest-Neighbour Ratio ($R_n$) | Z-score | Spatial Pattern |
|---|---|---|---|---|
| -1750 ms | Sinkholes formed above first karstification event in Oligocene/ Early Miocene, evidence for the presence of gas. | 0.845 | -10.36 | Clustered |
| -1150 ms | Late Miocene, multiple vertical dim zones. | 0.583 | -35.21 | Clustered |
| -950 ms | In Unit 5, gas pipes emanate from Miocene platforms and buildups, as well as from Miocene faults, some terminating as pockmarks. | 0.596 | -25.95 | Clustered |
| -650 ms | Unit 6, fewer gas pipes and pockmarks reach the shallowest Quaternary units, a few larger pipes extrude at the seafloor on the diapir flanks. | 0.534 | -15.78 | Clustered |
| -650 to -1900 ms | All fluid flow features recorded. | 0.760 | -48.68 | Clustered |

Table 2

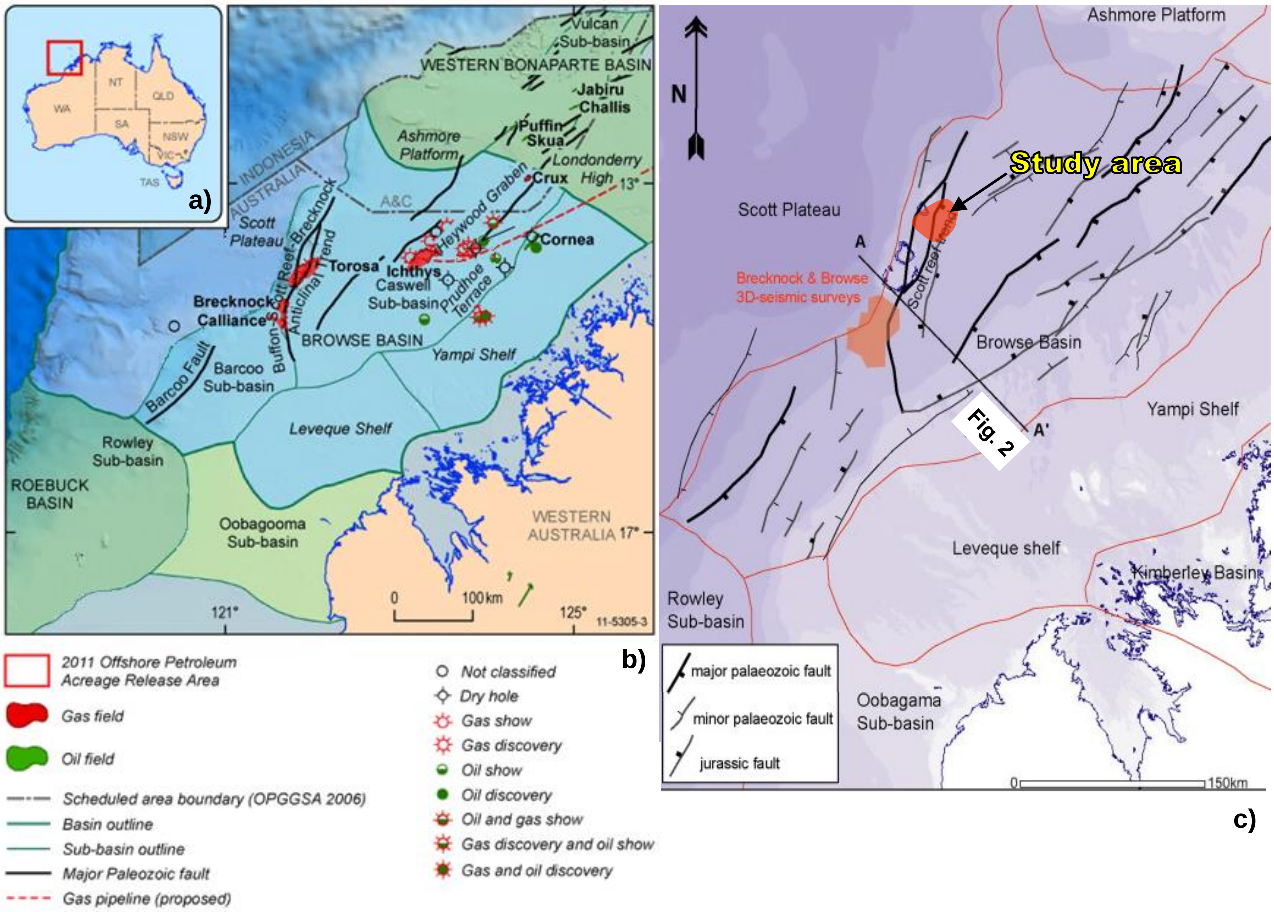

a)
b)
c)
Study area
Scott Plateau
Brecknock & Browse 3D-seismic surveys
Scott reef trend
Browse Basin
Yampi Shelf
Leveque shelf
Ashmore Platform
Kimberley Basin
Rowley Sub-basin
Oobagama Sub-basin
Fig. 2
A
A'
N
major palaeozoic fault
minor palaeozoic fault
jurassic fault
150km
WESTERN BONAPARTE BASIN
Vulcan Sub-basin
Ashmore Platform
Londonderry High
BROWSE BASIN
Caswell Sub-basin
Barcoo Sub-basin
Barcoo Fault
Leveque Shelf
Rowley Sub-basin
ROEBUCK BASIN
Oobagooma Sub-basin
WESTERN AUSTRALIA
Brecknock
Calliance
Torosa
Ichthys
Cornea
Crux
100 km
2011 Offshore Petroleum Acreage Release Area
Gas field
Oil field
Scheduled area boundary (OPGGSA 2006)
Basin outline
Sub-basin outline
Major Paleozoic fault
Gas pipeline (proposed)
Not classified
Dry hole
Gas show
Gas discovery
Oil show
Oil discovery
Oil and gas show
Gas discovery and oil show
Gas and oil discovery


Figure 1

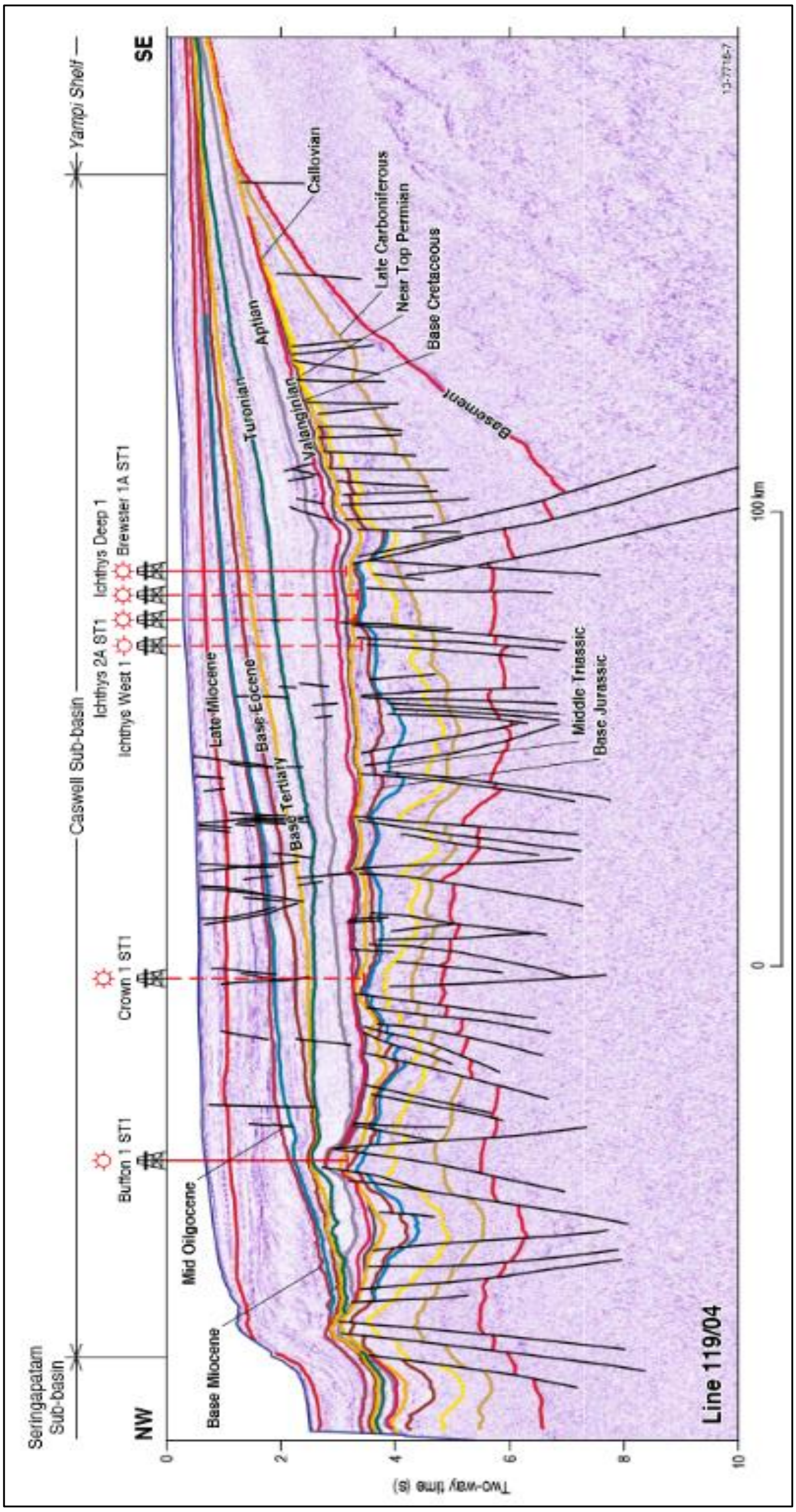

A
A'
Seringapatam Sub-basin
Caswell Sub-basin
Yampi Shelf
NW
SE
Buffon 1 ST1
Crown 1 ST1
Ichthys West 1
Ichthys 2A ST1
Ichthys Deep 1
Brewster 1A ST1
Base Miocene
Mid Oligocene
Late Miocene
Base Eocene
Base Tertiary
Turonian
Aptian
Valanginian
Callovian
Late Carboniferous
Near Top Permian
Base Cretaceous
Basement
Middle Triassic
Base Jurassic
Line 119/04
Two-way time (s)
0
2
4
6
8
10
0
100 km


Figure 2

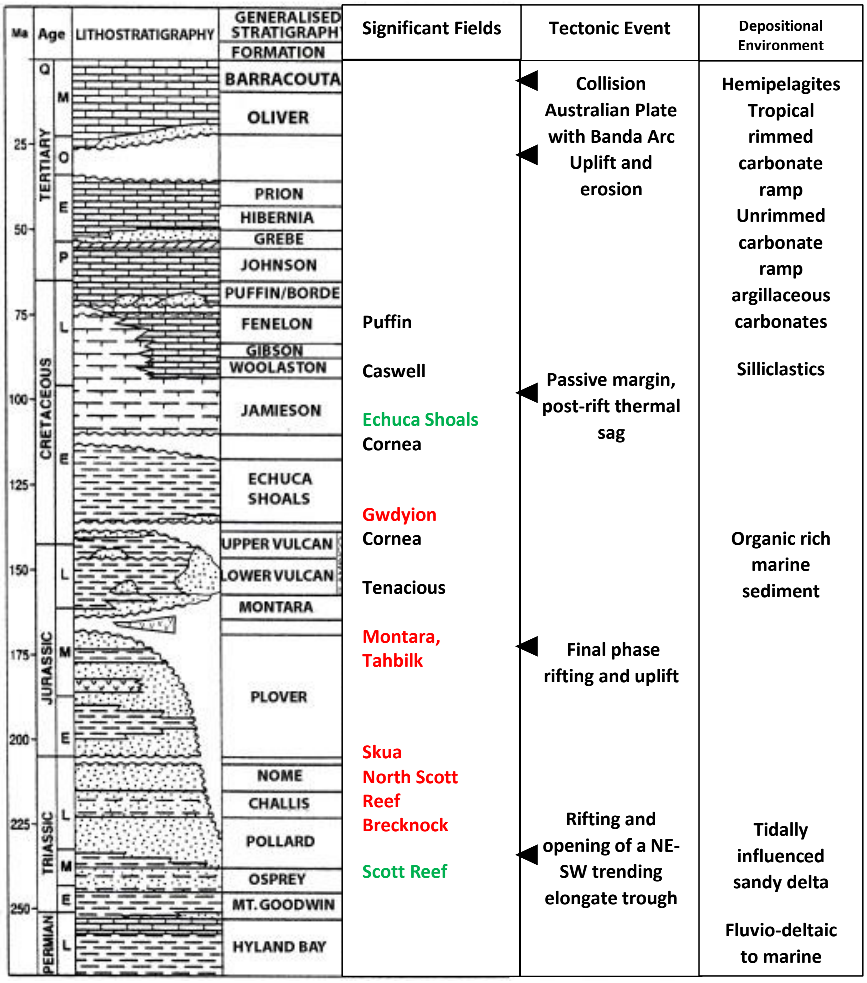

Ma
Age
LITHOSTRATIGRAPHY
GENERALISED STRATIGRAPHY FORMATION
Significant Fields
Tectonic Event
Depositional Environment
25
50
75
100
125
150
175
200
225
250
TERTIARY
CRETACEOUS
JURASSIC
TRIASSIC
PERMIAN
Q
M
O
E
P
L
E
L
M
E
L
M
E
L
BARRACOUTA
OLIVER
PRION
HIBERNIA
GREBE
JOHNSON
PUFFIN/BORDE
FENELON
GIBSON
WOOLASTON
JAMIESON
ECHUCA SHOALS
UPPER VULCAN
LOWER VULCAN
MONTARA
PLOVER
NOME
CHALLIS
POLLARD
OSPREY
MT. GOODWIN
HYLAND BAY
Puffin
Caswell
Echuca Shoals
Cornea
Gwdyion
Cornea
Tenacious
Montara, Tahbilk
Skua
North Scott Reef
Brecknock
Scott Reef
Collision Australian Plate with Banda Arc Uplift and erosion
Passive margin, post-rift thermal sag
Final phase rifting and uplift
Rifting and opening of a NE-SW trending elongate trough
Hemipelagites
Tropical rimmed carbonate ramp
Unrimmed carbonate ramp
argillaceous carbonates
Silliclastics
Organic rich marine sediment
Tidally influenced sandy delta
Fluvio-deltaic to marine


Figure 3

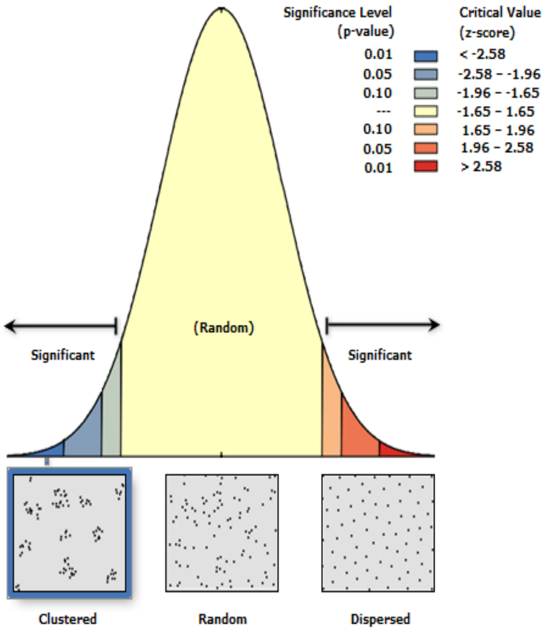
Significance Level
(p-value)
Critical Value
(z-score)
0.01
< -2.58
0.05
-2.58 - -1.96
0.10
-1.96 - -1.65
---
-1.65 - 1.65
0.10
1.65 - 1.96
0.05
1.96 - 2.58
0.01
> 2.58
Significant
(Random)
Significant
Clustered
Random
Dispersed

Figure 4

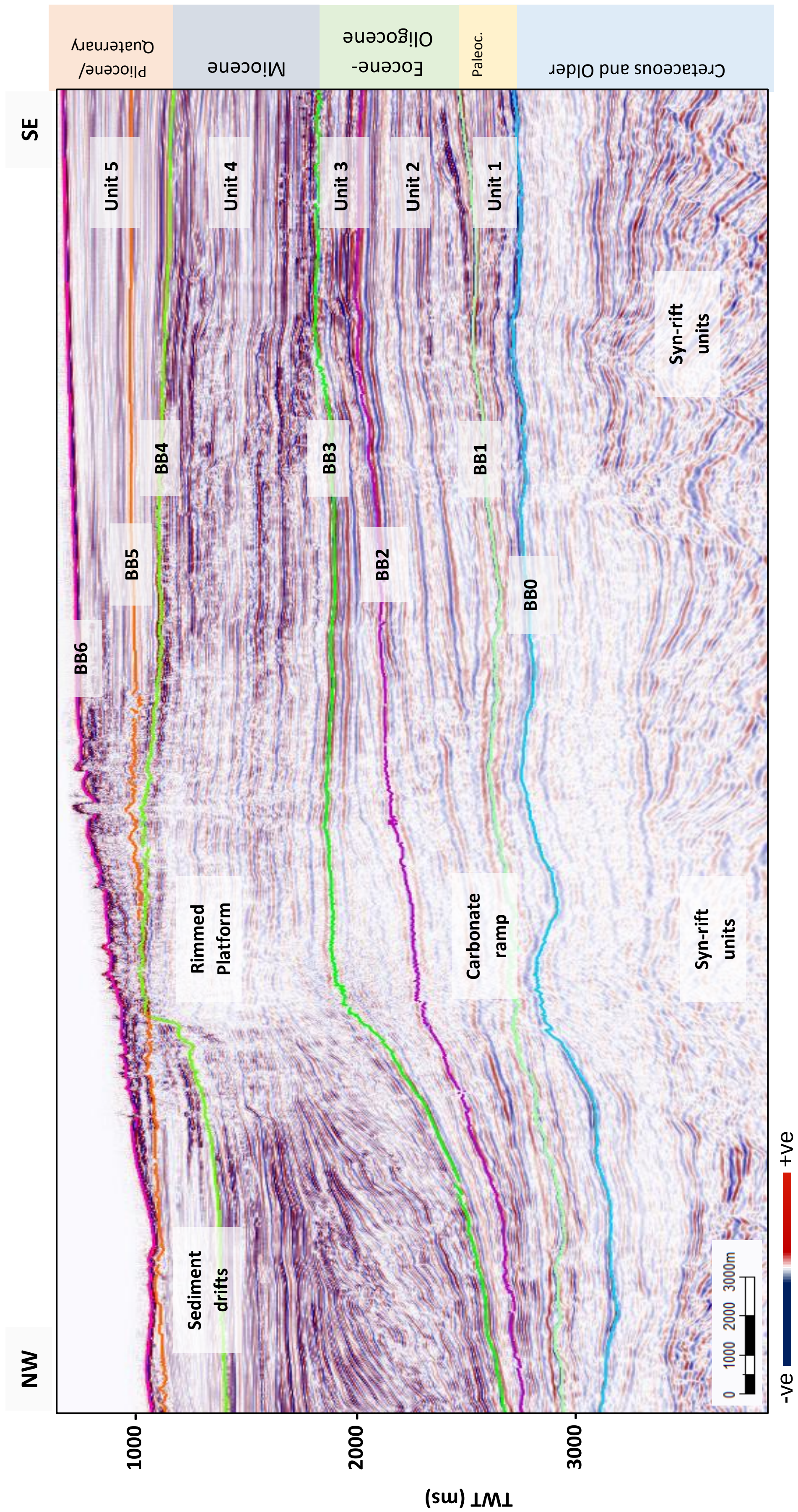

NW
SE
Pliocene/ Quaternary
Miocene
Eocene- Oligocene
Paleoc.
Cretaceous and Older
Unit 5
Unit 4
Unit 3
Unit 2
Unit 1
BB6
BB5
BB4
BB3
BB2
BB1
BB0
Sediment drifts
Rimmed Platform
Carbonate ramp
Syn-rift units
Syn-rift units
TWT (ms)
1000
2000
3000
0 1000 2000 3000m
-ve
+ve


Figure 5

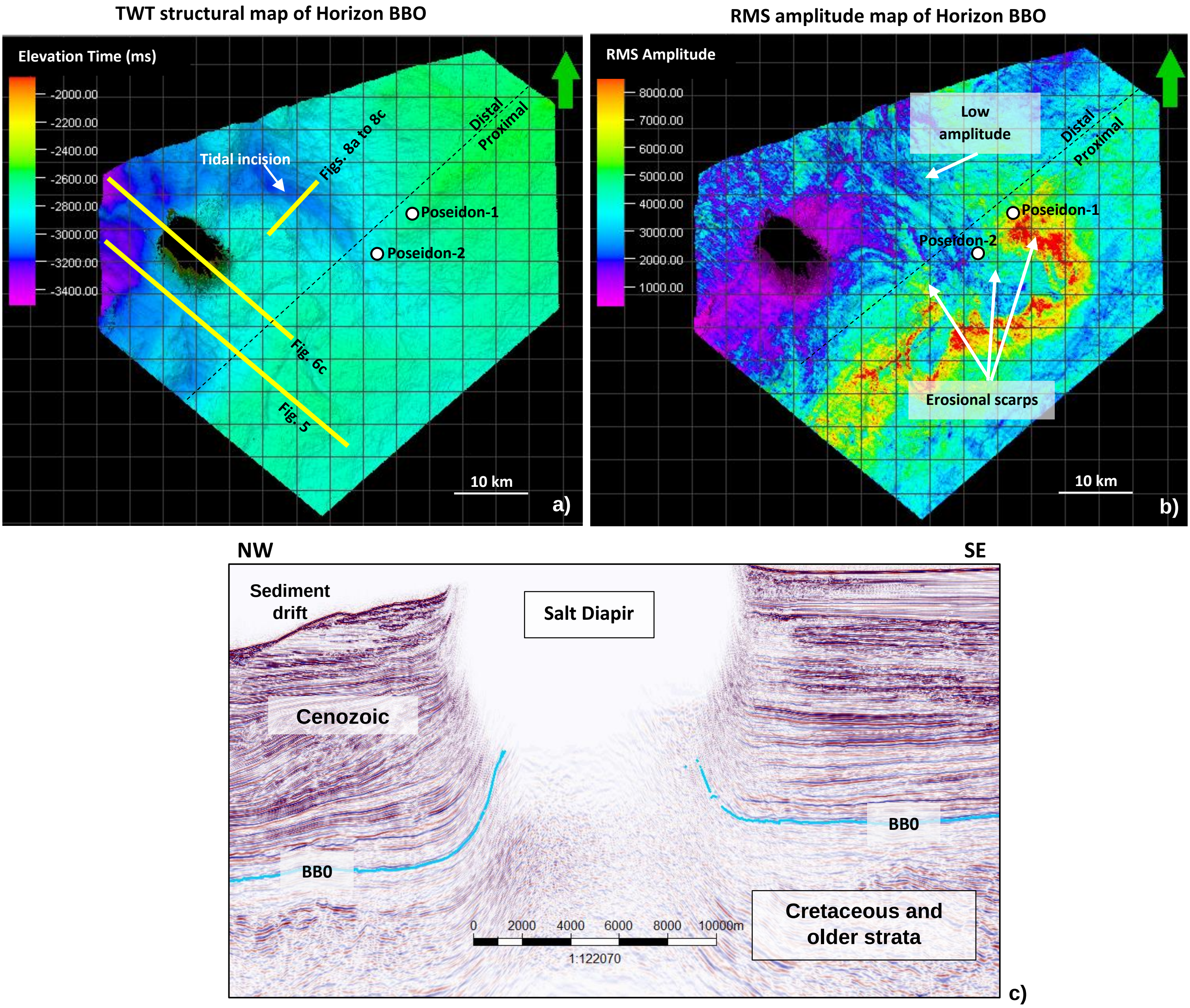
TWT structural map of Horizon BBO
Elevation Time (ms)
-2000.00
-2200.00
-2400.00
-2600.00
-2800.00
-3000.00
-3200.00
-3400.00
Tidal incision
Figs. 8a to 8c
Distal
Proximal
Poseidon-1
Poseidon-2
Fig. 6c
Fig. 5
10 km
a)
RMS amplitude map of Horizon BBO
RMS Amplitude
8000.00
7000.00
6000.00
5000.00
4000.00
3000.00
2000.00
1000.00
Low amplitude
Distal
Proximal
Poseidon-1
Poseidon-2
Erosional scarps
10 km
b)
NW
SE
Sediment drift
Salt Diapir
Cenozoic
BB0
BB0
Cretaceous and older strata
0 2000 4000 6000 8000 10000m
1:122070
c)

Figure 6

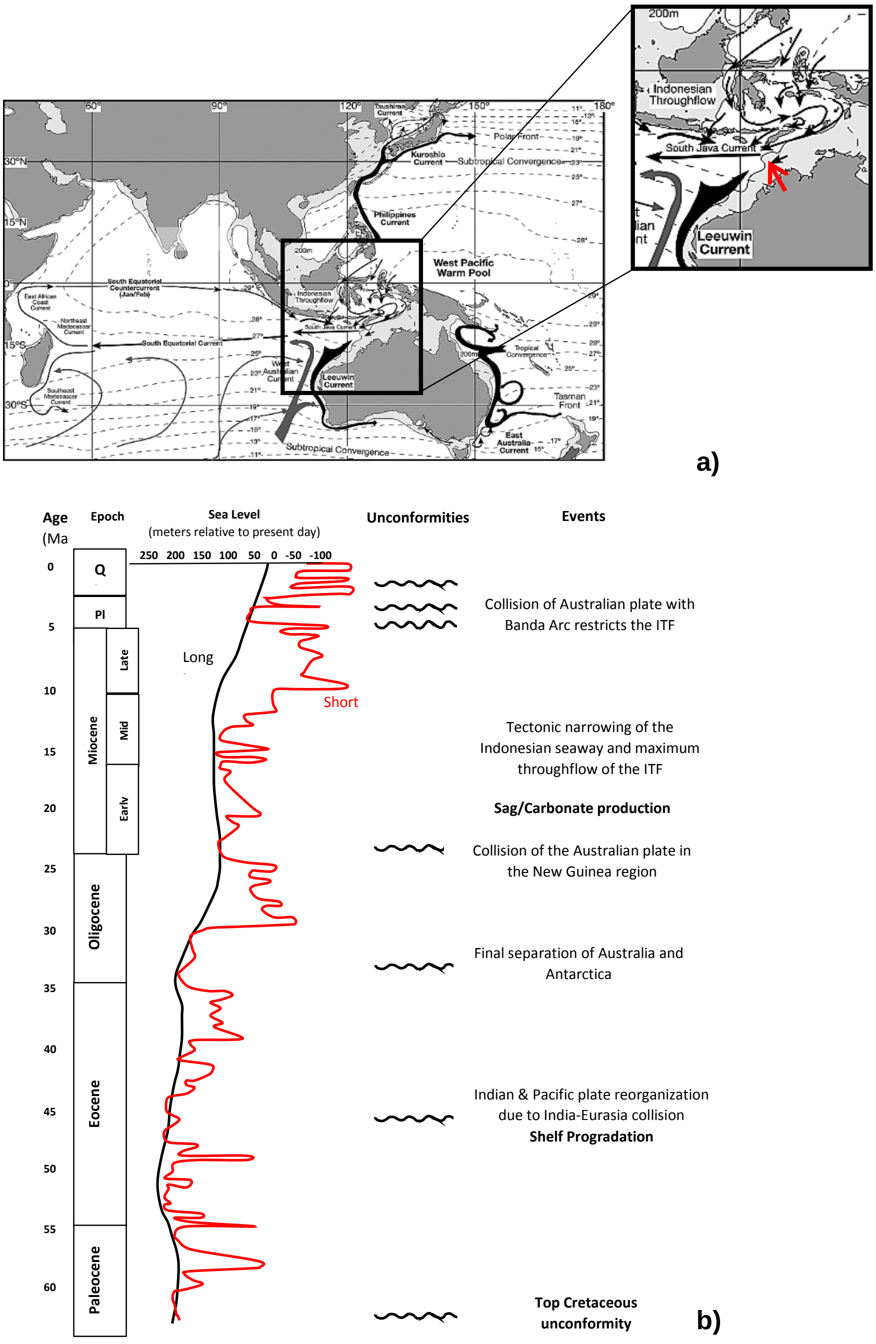

a)
Indonesian Throughflow
South Java Current
Leeuwin Current
West Australian Current
Kuroshio Current
Philippines Current
West Pacific Warm Pool
Polar Front
Subtropical Convergence
South Equatorial Countercurrent
South Equatorial Current
Tropical Convergence
Tasman Front
East Australia Current
b)
Age (Ma
Epoch
Sea Level
(meters relative to present day)
250 200 150 100 50 0 -50 -100
Unconformities
Events
Q
Pl
Miocene
Late
Mid
Early
Oligocene
Eocene
Paleocene
Long
Short
Collision of Australian plate with Banda Arc restricts the ITF
Tectonic narrowing of the Indonesian seaway and maximum throughflow of the ITF
Sag/Carbonate production
Collision of the Australian plate in the New Guinea region
Final separation of Australia and Antarctica
Indian & Pacific plate reorganization due to India-Eurasia collision
Shelf Progradation
Top Cretaceous unconformity


Figure 7

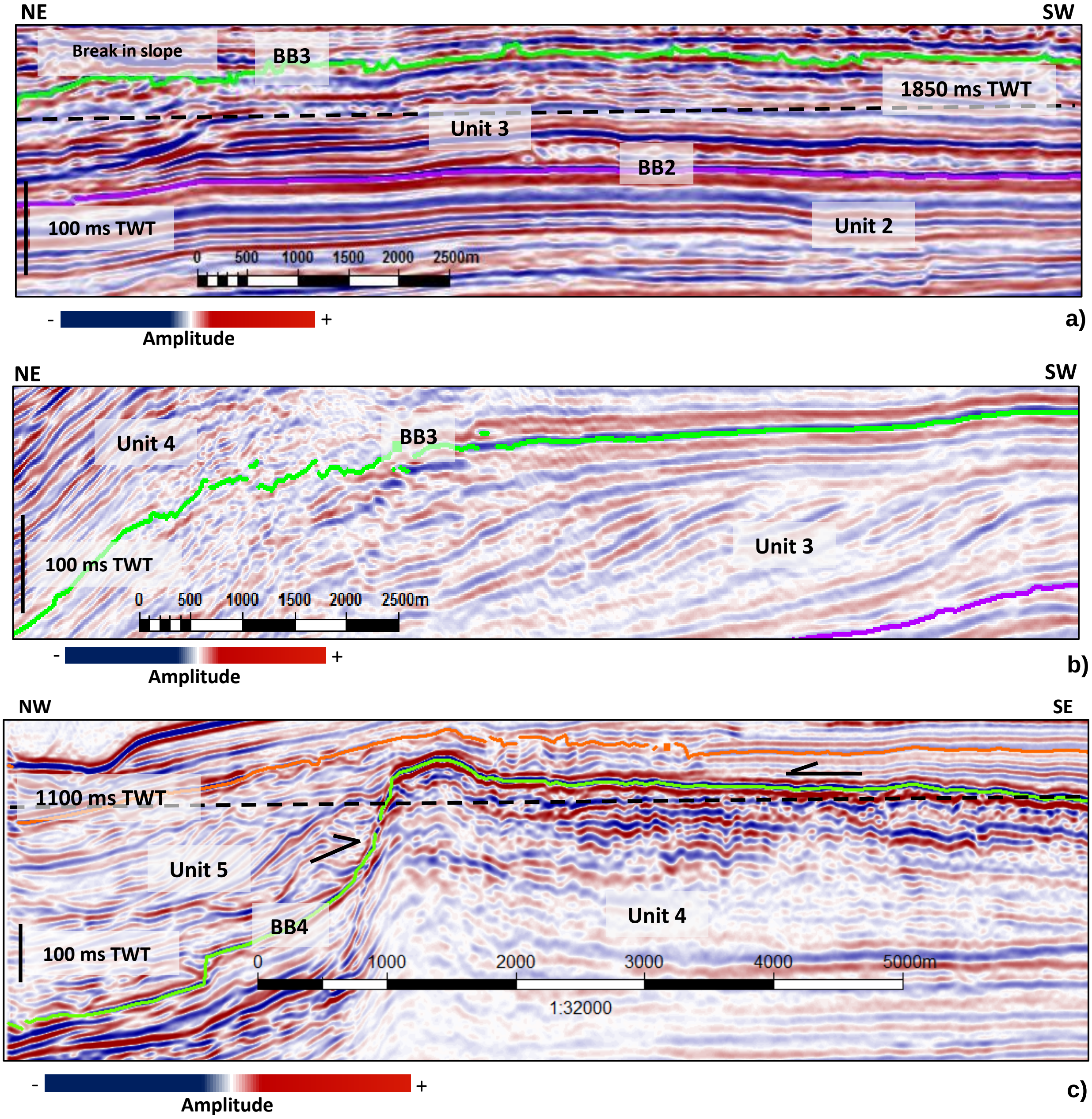
NE
SW
Break in slope
BB3
1850 ms TWT
Unit 3
BB2
100 ms TWT
Unit 2
0 500 1000 1500 2000 2500m
-
+
Amplitude
a)
NE
SW
Unit 4
BB3
Unit 3
100 ms TWT
0 500 1000 1500 2000 2500m
-
+
Amplitude
b)
NW
SE
1100 ms TWT
Unit 5
BB4
Unit 4
100 ms TWT
0 1000 2000 3000 4000 5000m
1:32000
-
+
Amplitude
c)

Figure 8

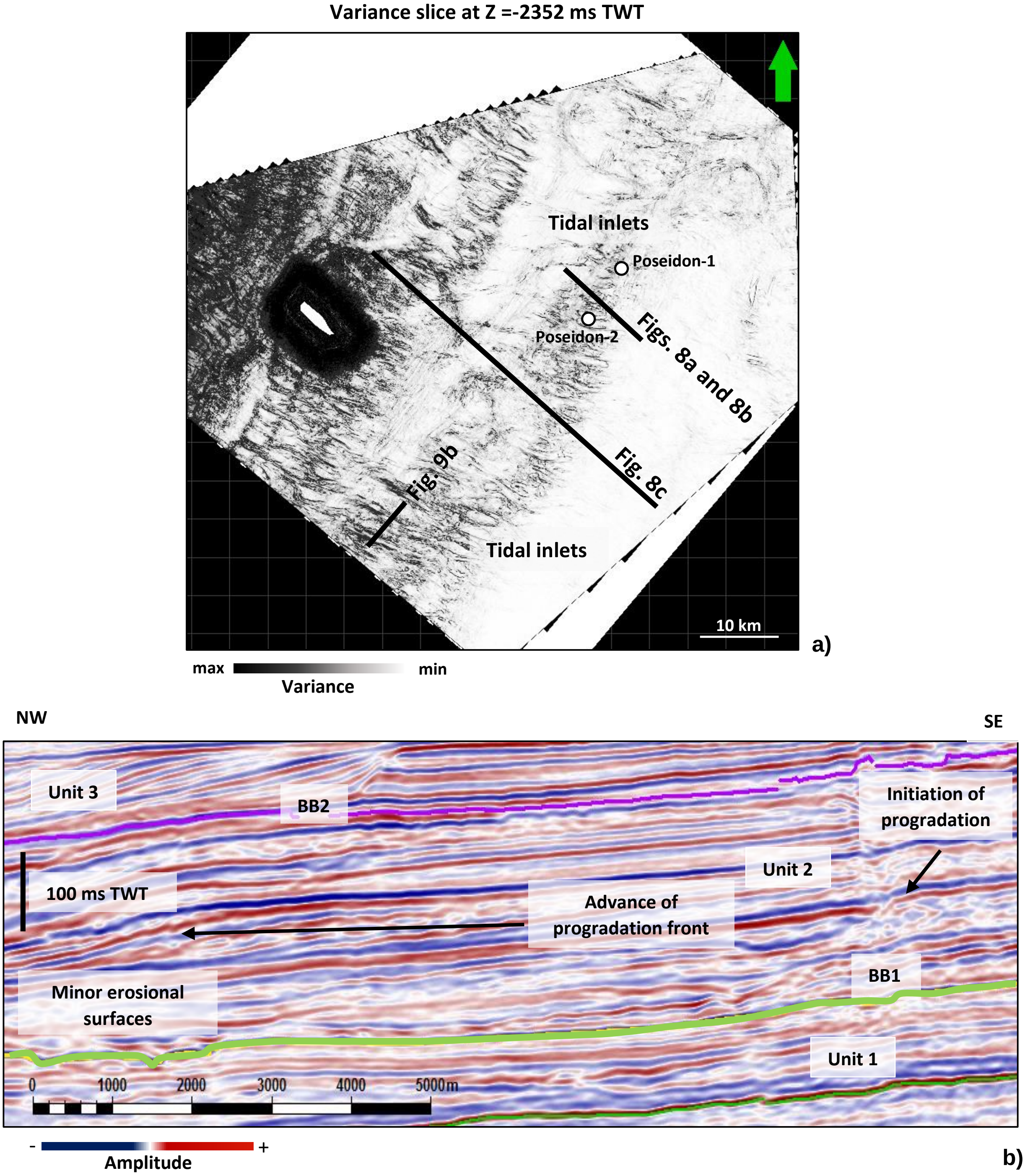

Variance slice at Z =-2352 ms TWT
Tidal inlets
Poseidon-1
Poseidon-2
Figs. 8a and 8b
Fig. 8c
Fig. 9b
Tidal inlets
10 km
a)
max
min
Variance
NW
SE
Unit 3
BB2
Initiation of progradation
Unit 2
100 ms TWT
Advance of progradation front
Minor erosional surfaces
BB1
Unit 1
0
1000
2000
3000
4000
5000m
-
+
Amplitude
b)


Figure 9

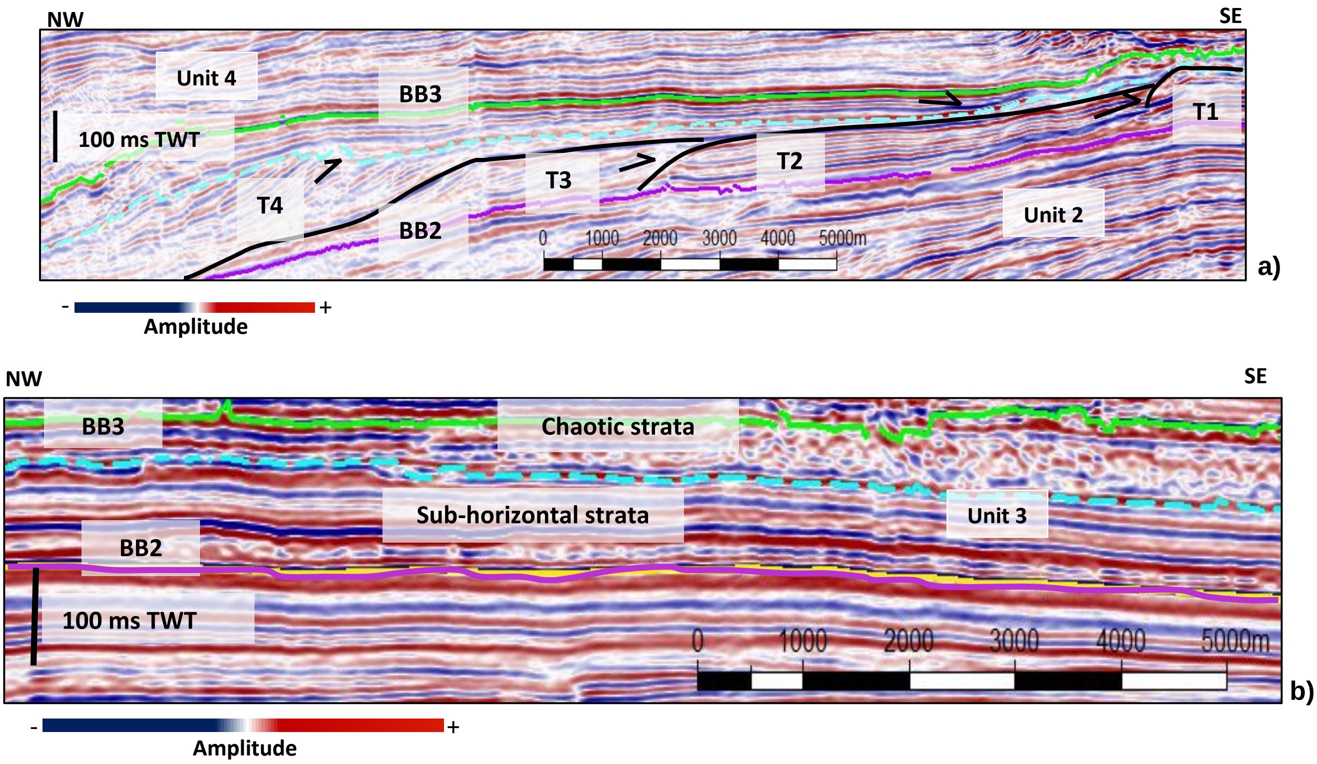
NW
SE
Unit 4
BB3
100 ms TWT
T1
T2
T3
T4
BB2
Unit 2
0
1000
2000
3000
4000
5000m
a)
-
+
Amplitude
NW
SE
BB3
Chaotic strata
Sub-horizontal strata
Unit 3
BB2
100 ms TWT
0
1000
2000
3000
4000
5000m
b)
-
+
Amplitude

Figure 10

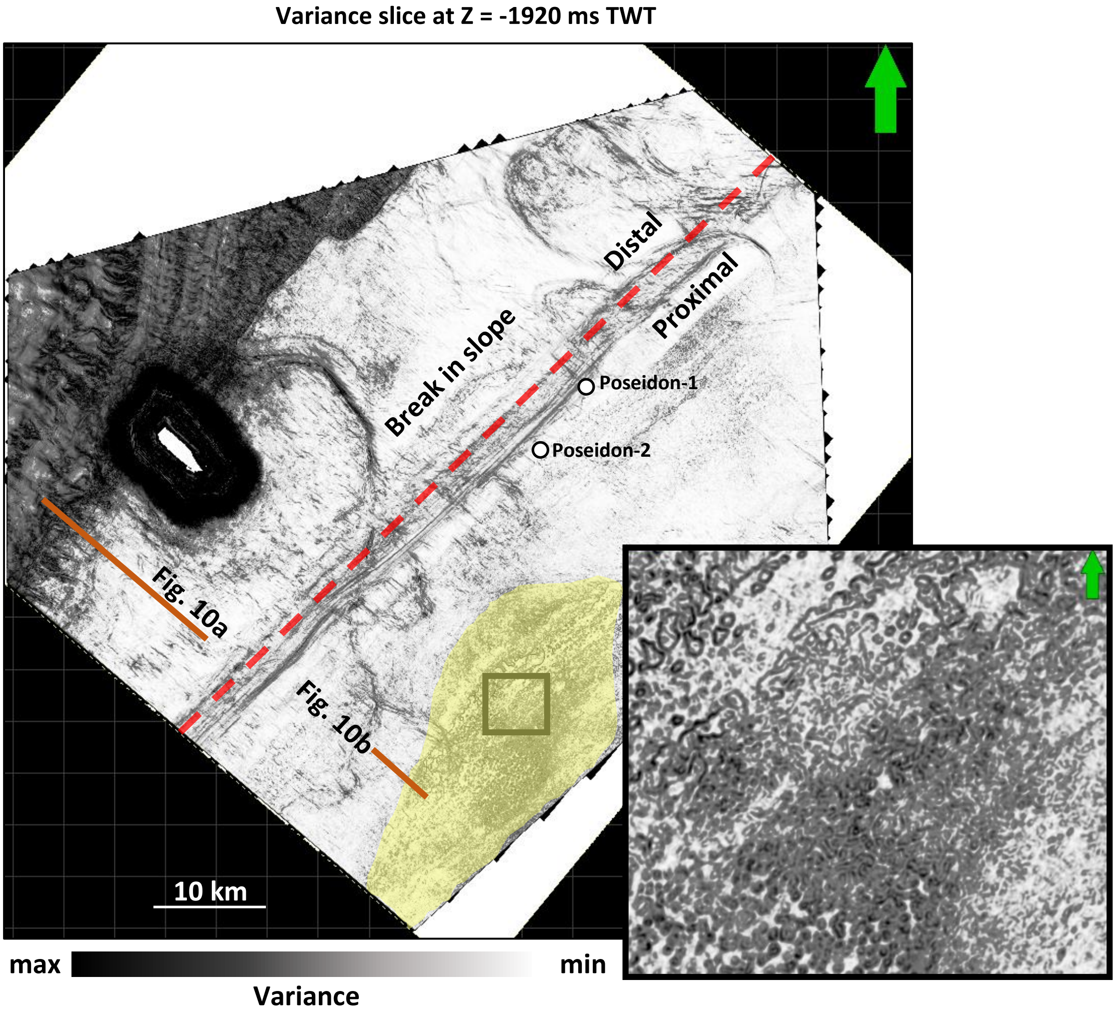
Variance slice at Z = -1920 ms TWT
Distal
Proximal
Break in slope
Poseidon-1
Poseidon-2
Fig. 10a
Fig. 10b
10 km
max
min
Variance

Figure 11

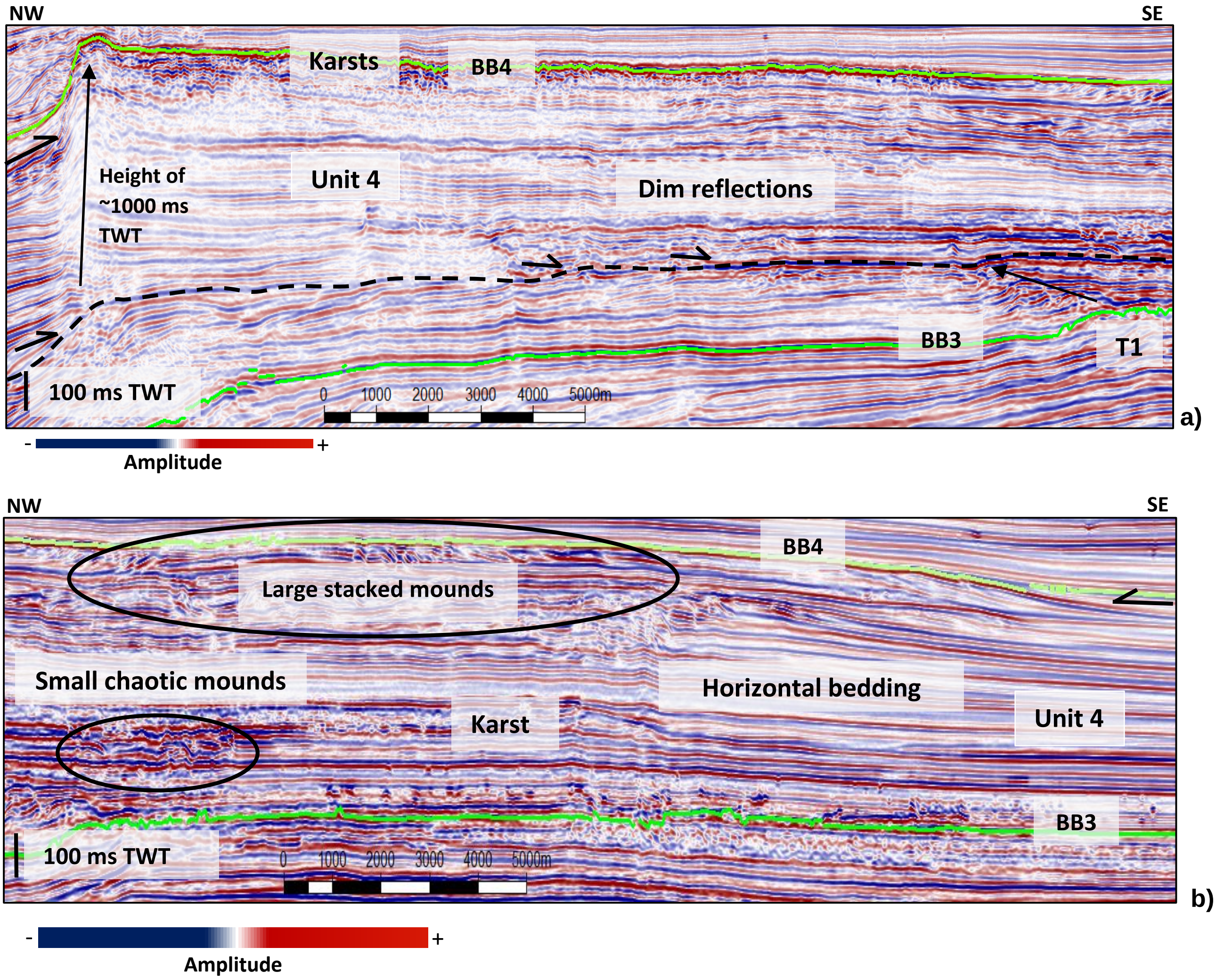

NW
SE
Karsts
BB4
Height of
~1000 ms
TWT
Unit 4
Dim reflections
BB3
T1
100 ms TWT
0 1000 2000 3000 4000 5000m
a)
- Amplitude +
NW
SE
BB4
Large stacked mounds
Small chaotic mounds
Karst
Horizontal bedding
Unit 4
BB3
100 ms TWT
0 1000 2000 3000 4000 5000m
b)
- Amplitude +


Figure 12

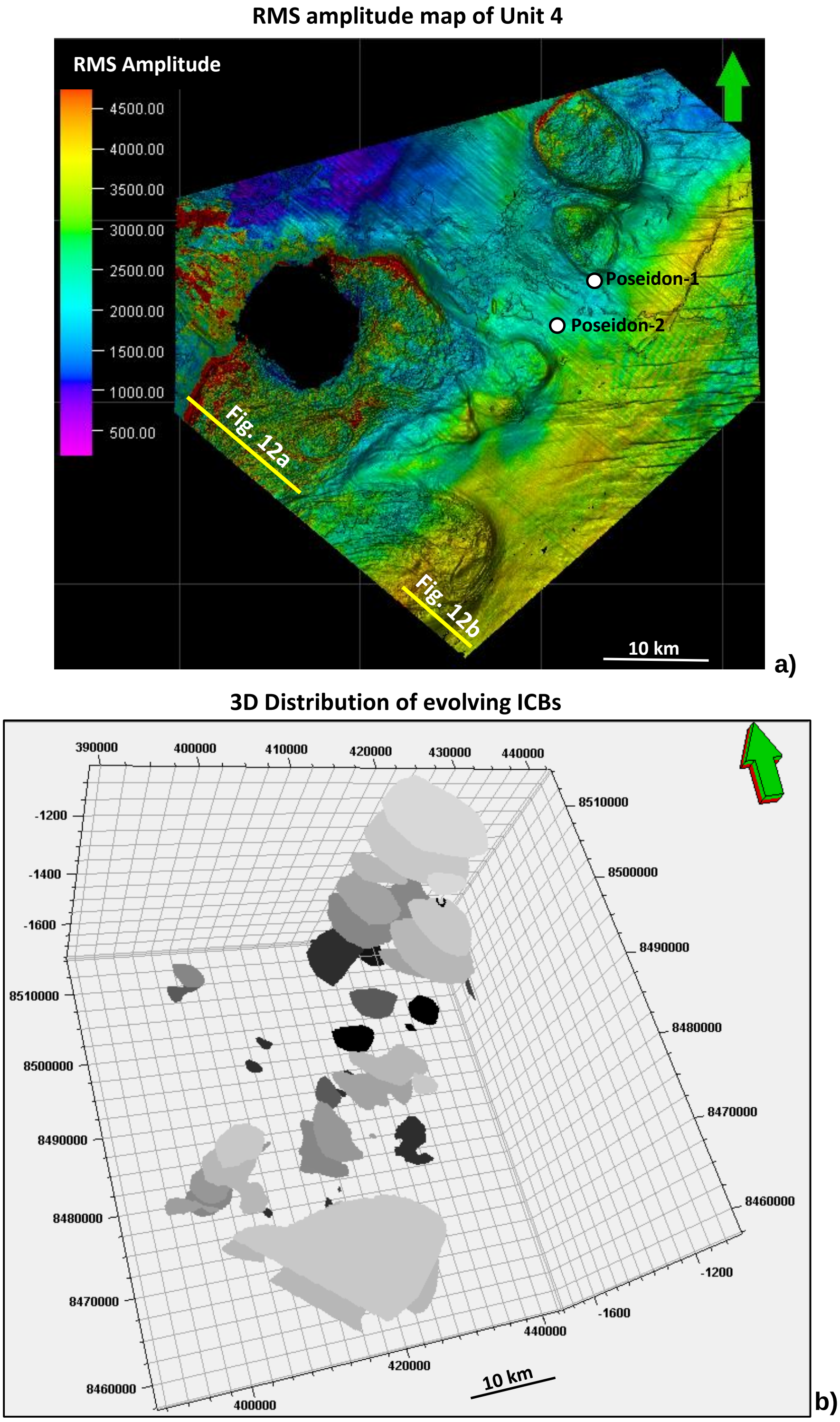
RMS amplitude map of Unit 4
RMS Amplitude
4500.00
4000.00
3500.00
3000.00
2500.00
2000.00
1500.00
1000.00
500.00
Poseidon-1
Poseidon-2
Fig. 12a
Fig. 12b
10 km
a)
3D Distribution of evolving ICBs
390000
400000
410000
420000
430000
440000
8510000
8500000
8490000
8480000
8470000
8460000
-1200
-1400
-1600
10 km
b)

Figure 13

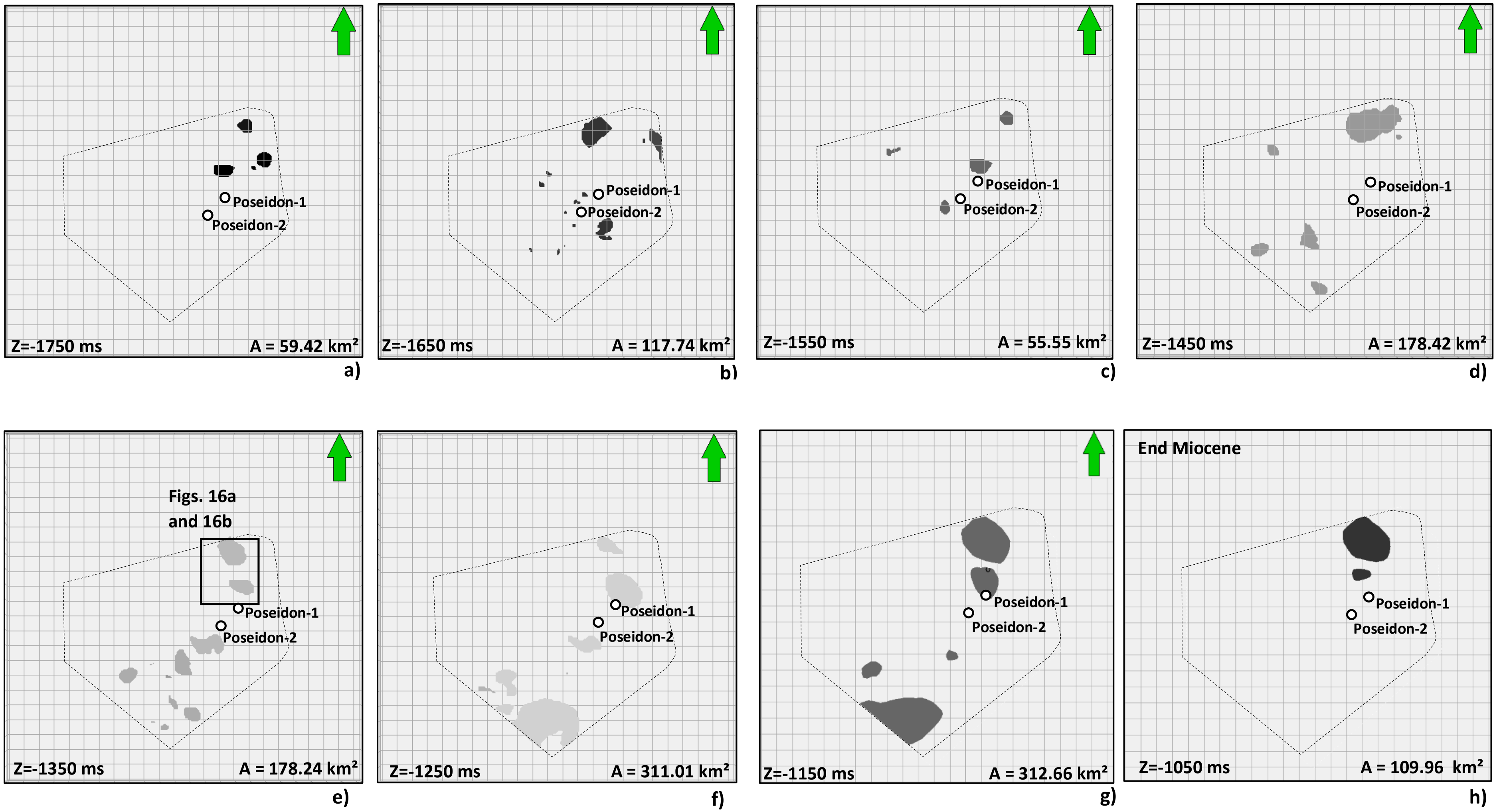

Poseidon-1
Poseidon-2
Z=-1750 ms
A = 59.42 km²
a)
Z=-1650 ms
A = 117.74 km²
b)
Z=-1550 ms
A = 55.55 km²
c)
Z=-1450 ms
A = 178.42 km²
d)
Figs. 16a
and 16b
Z=-1350 ms
A = 178.24 km²
e)
Z=-1250 ms
A = 311.01 km²
f)
Z=-1150 ms
A = 312.66 km²
g)
End Miocene
Z=-1050 ms
A = 109.96 km²
h)


Figure 14

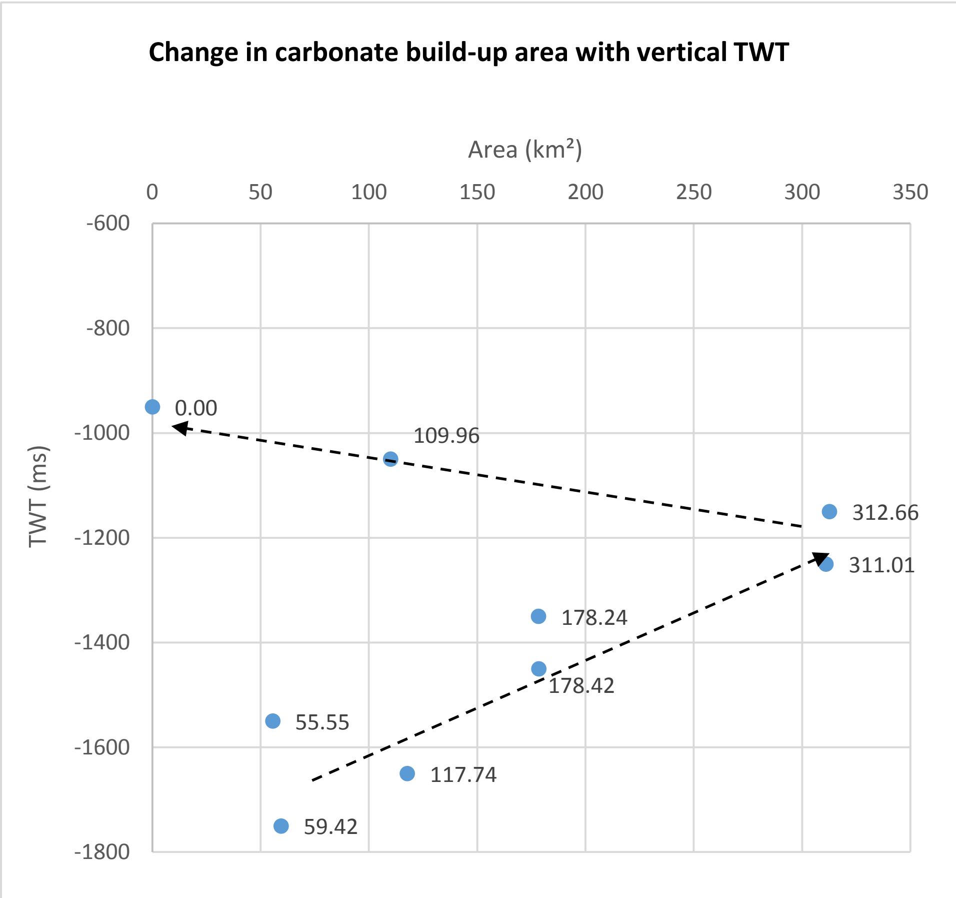
Change in carbonate build-up area with vertical TWT
Area (km²)
0
50
100
150
200
250
300
350
-600
-800
-1000
-1200
-1400
-1600
-1800
TWT (ms)
0.00
109.96
312.66
311.01
178.24
178.42
55.55
117.74
59.42

Figure 15

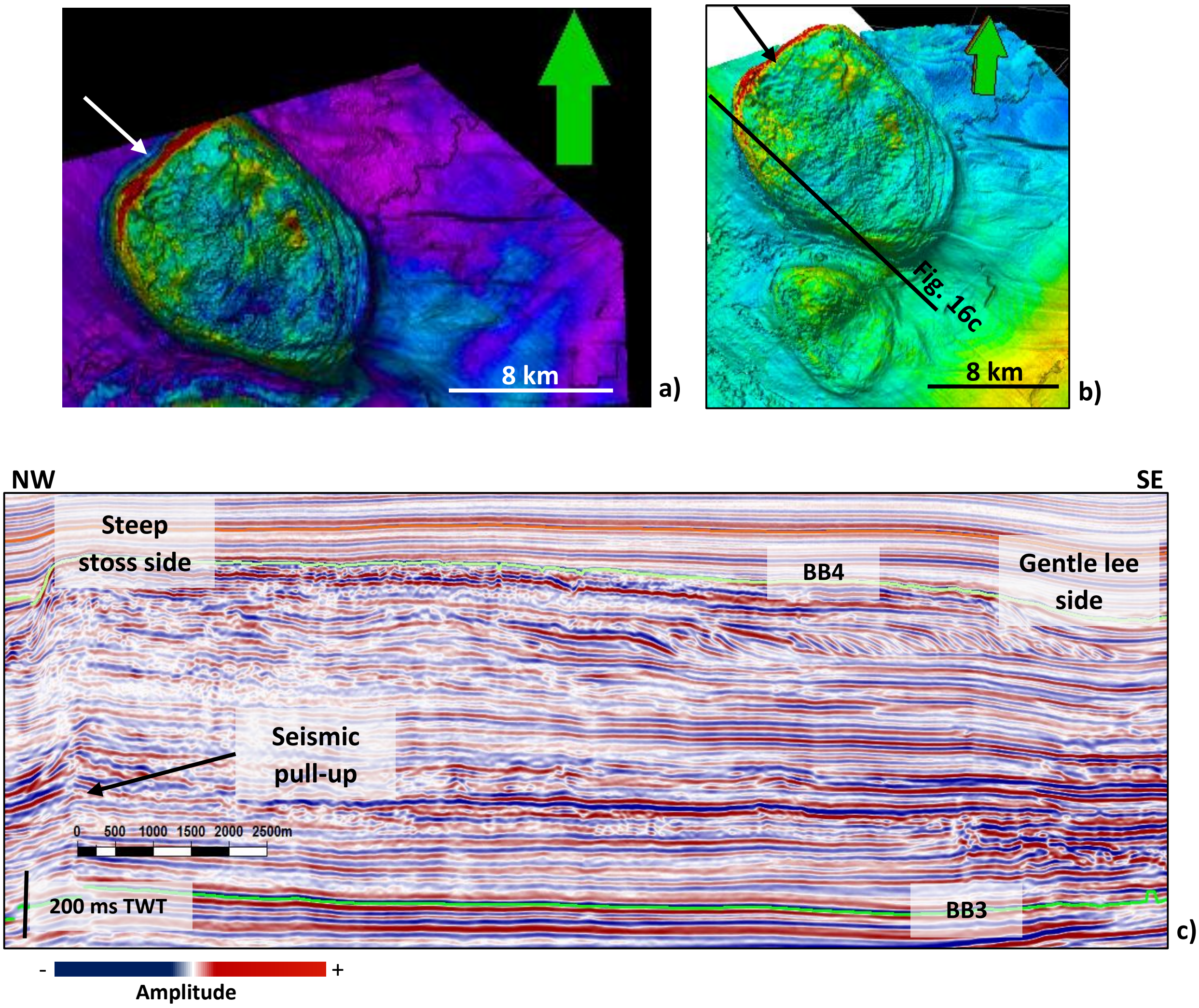
8 km
a)
Fig. 16c
8 km
b)
NW
SE
Steep
stoss side
BB4
Gentle lee
side
Seismic
pull-up
0 500 1000 1500 2000 2500m
200 ms TWT
BB3
c)
-
+
Amplitude

Figure 16

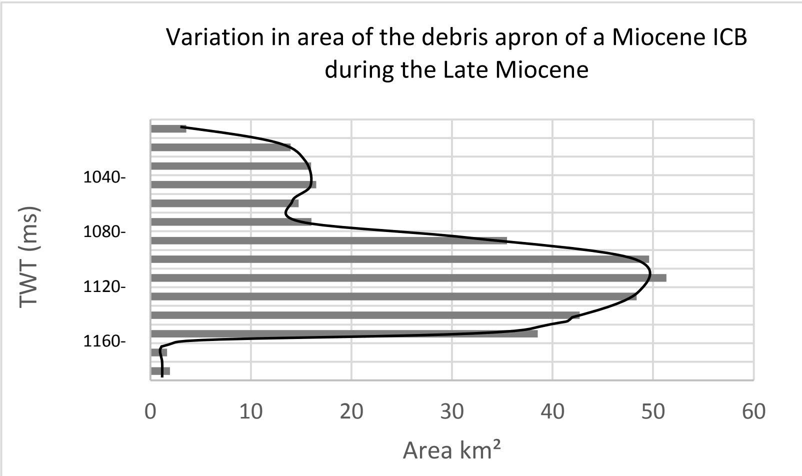
Variation in area of the debris apron of a Miocene ICB
during the Late Miocene
TWT (ms)
1040-
1080-
1120-
1160-
0
10
20
30
40
50
60
Area km²

Figure 17

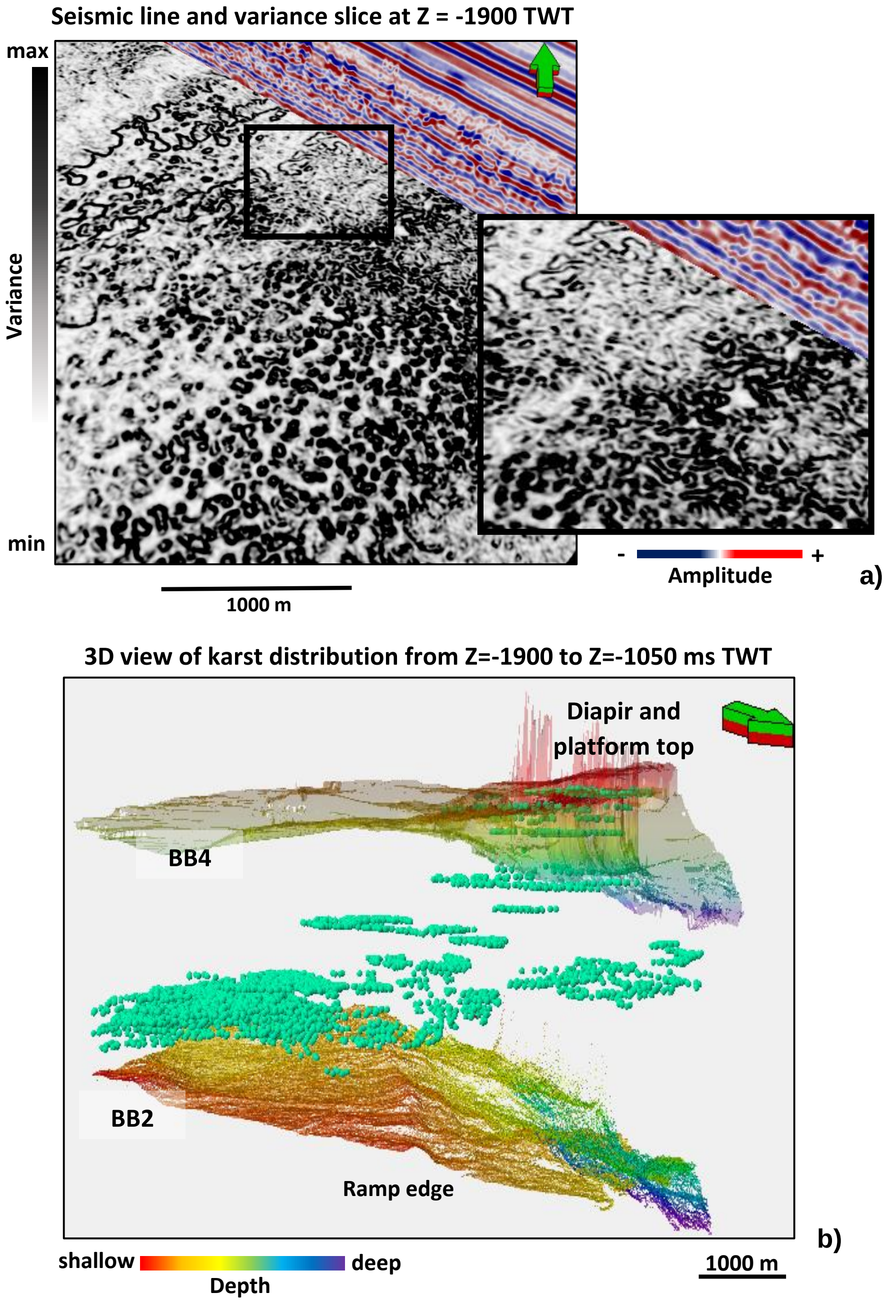
Seismic line and variance slice at Z = -1900 TWT
max
Variance
min
1000 m
-
+
Amplitude
a)
3D view of karst distribution from Z=-1900 to Z=-1050 ms TWT
Diapir and
platform top
BB4
BB2
Ramp edge
b)
shallow
deep
Depth
1000 m

Figure 18

Variance slice at Z=-1700 ms TWT

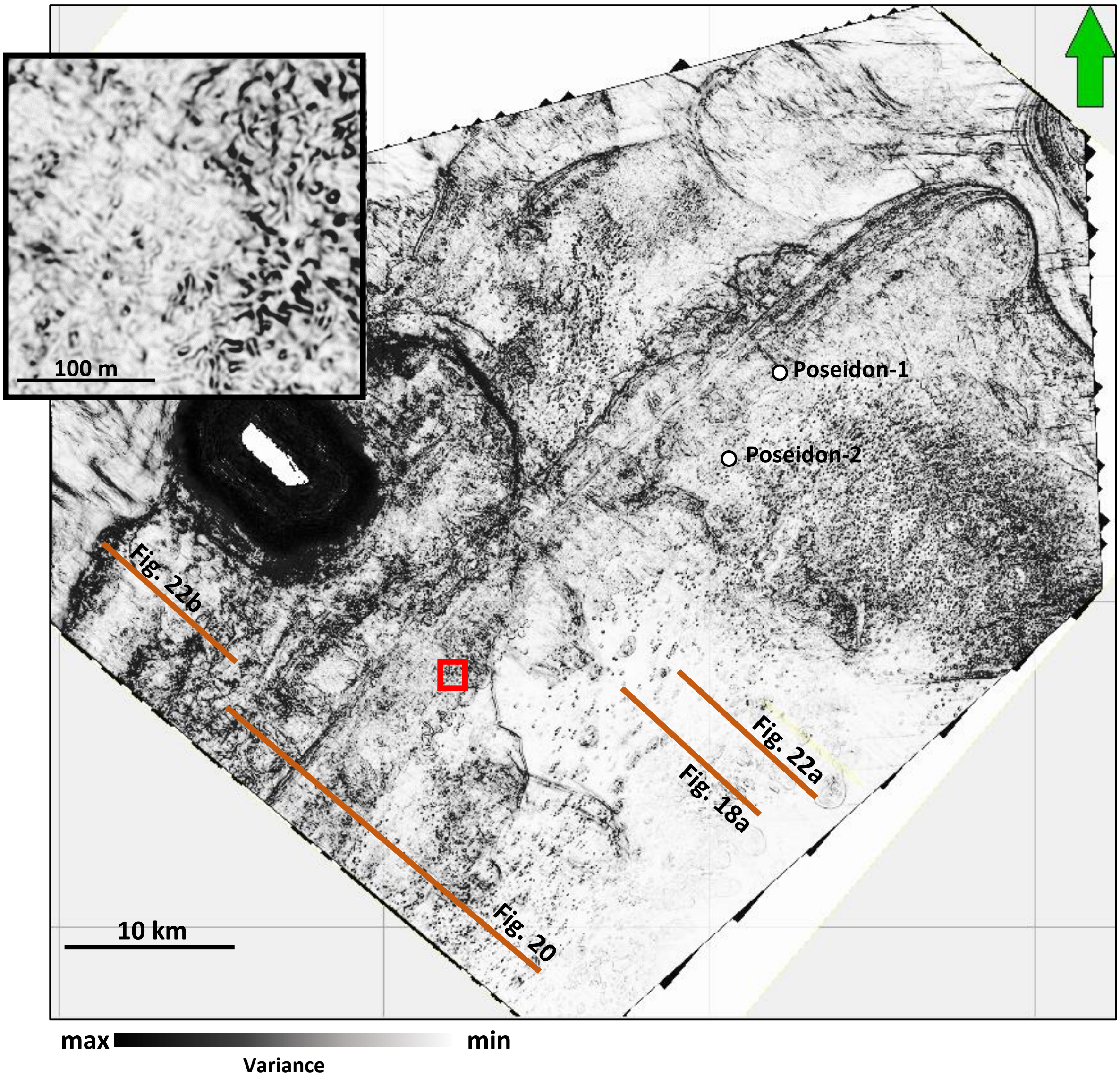


Figure 19

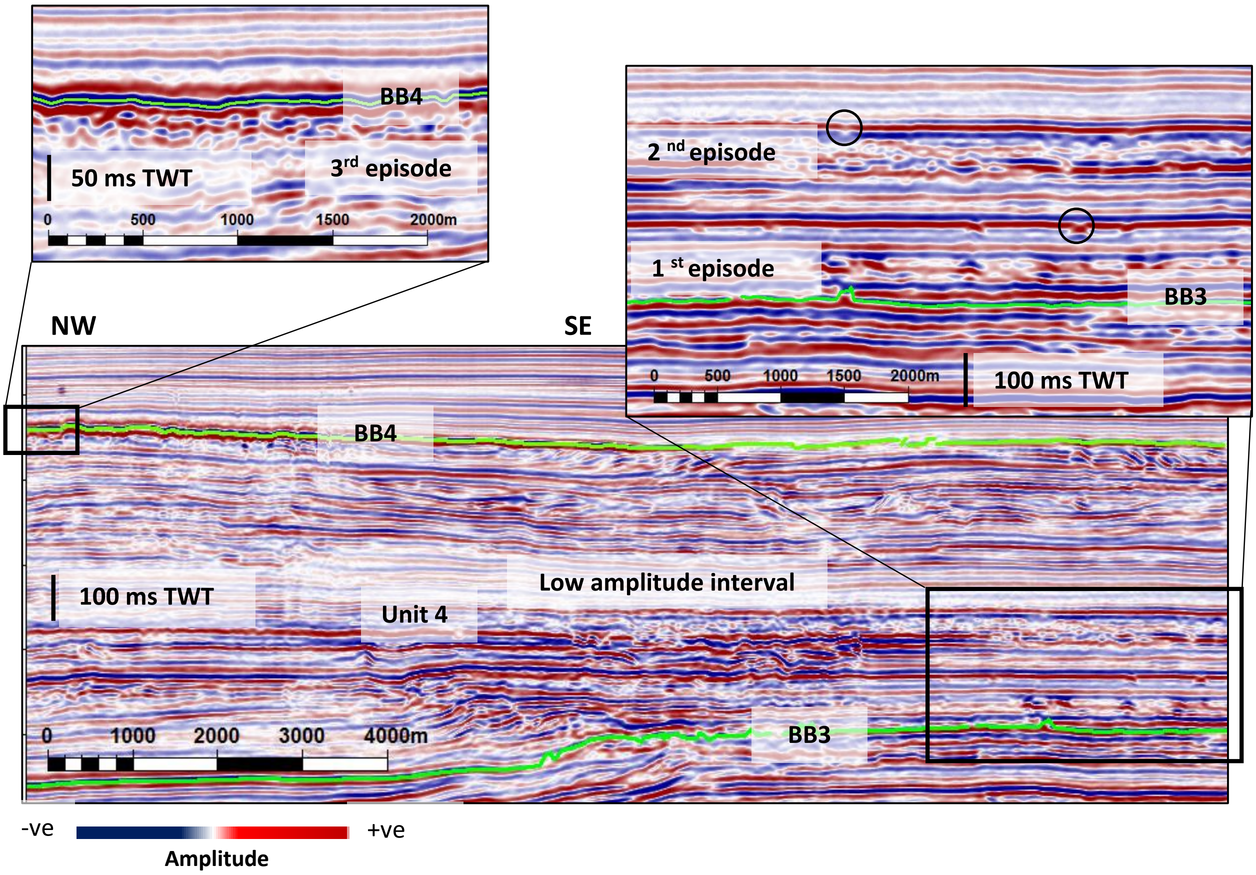

BB4
3rd episode
50 ms TWT
0
500
1000
1500
2000m
2 nd episode
1 st episode
BB3
0
500
1000
1500
2000m
100 ms TWT
NW
SE
BB4
100 ms TWT
Low amplitude interval
Unit 4
0
1000
2000
3000
4000m
BB3
-ve
+ve
Amplitude


Figure 20

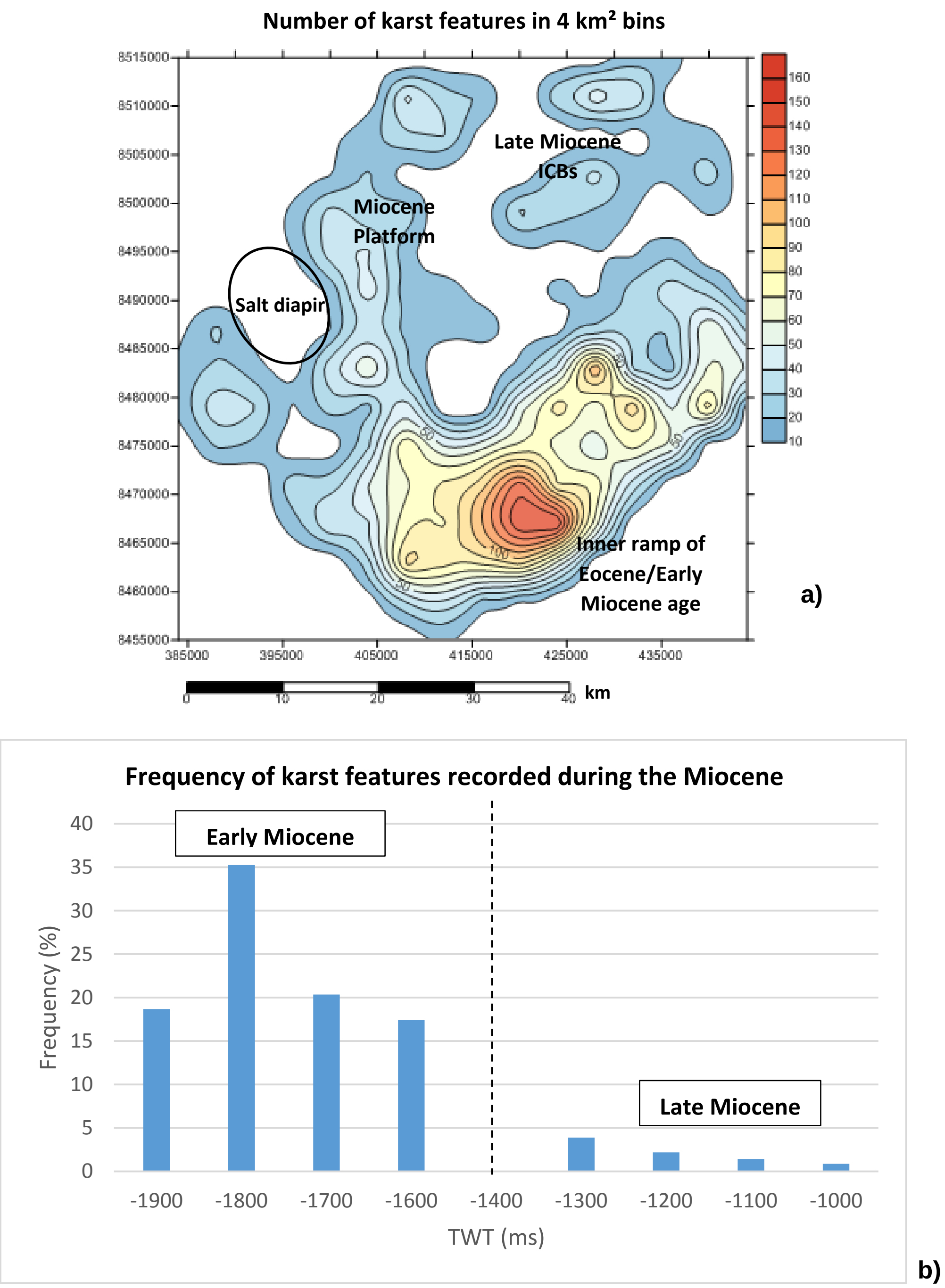
Number of karst features in 4 km² bins
Late Miocene
ICBs
Miocene
Platform
Salt diapir
Inner ramp of
Eocene/Early
Miocene age
km
a)
Frequency of karst features recorded during the Miocene
Early Miocene
Late Miocene
Frequency (%)
TWT (ms)
b)

Figure 21

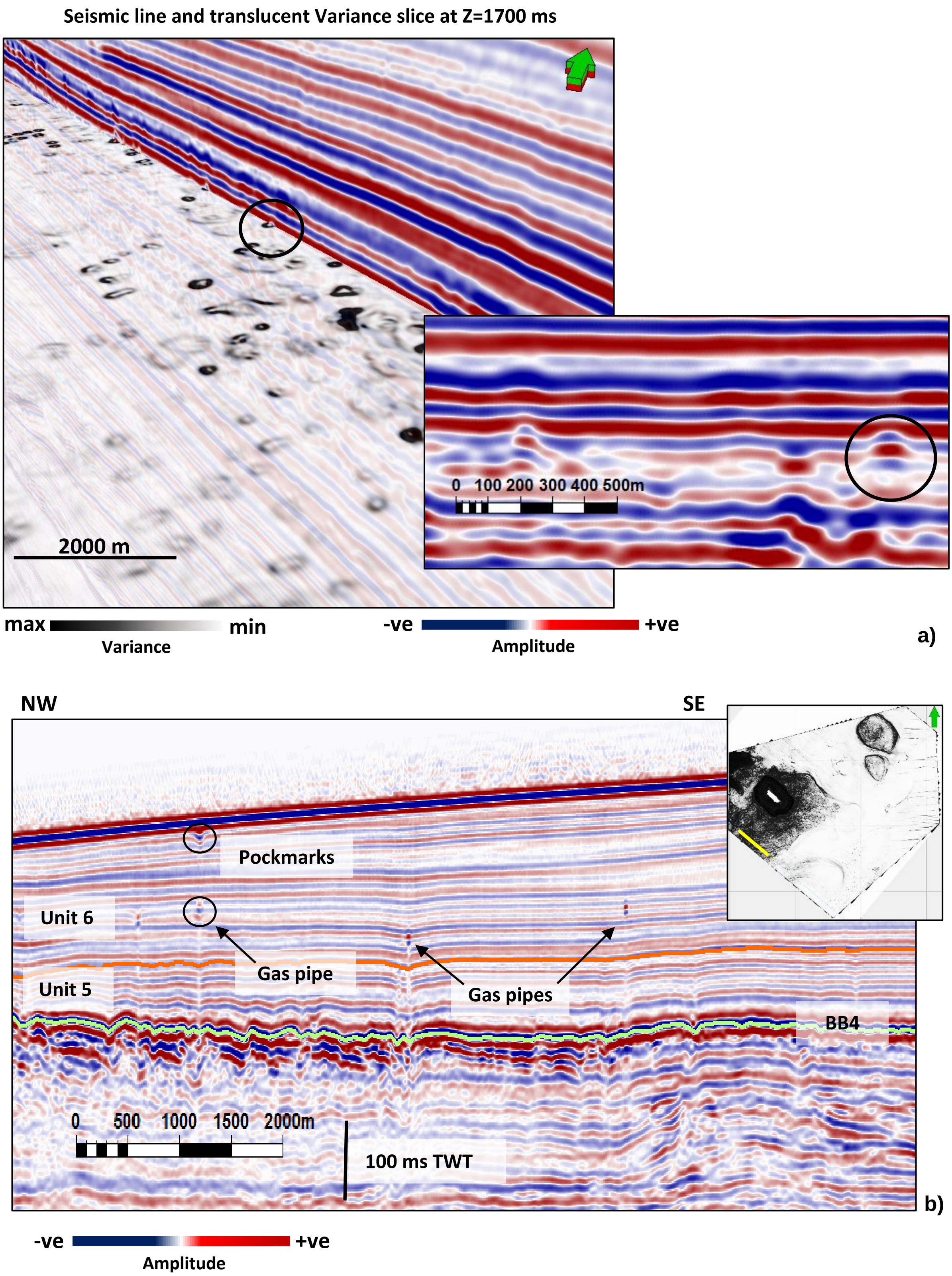

Seismic line and translucent Variance slice at Z=1700 ms
0 100 200 300 400 500m
2000 m
max
Variance
min
-ve
Amplitude
+ve
a)
NW
SE
Pockmarks
Unit 6
Gas pipe
Unit 5
Gas pipes
BB4
0 500 1000 1500 2000m
100 ms TWT
b)
-ve
Amplitude
+ve


Figure 22

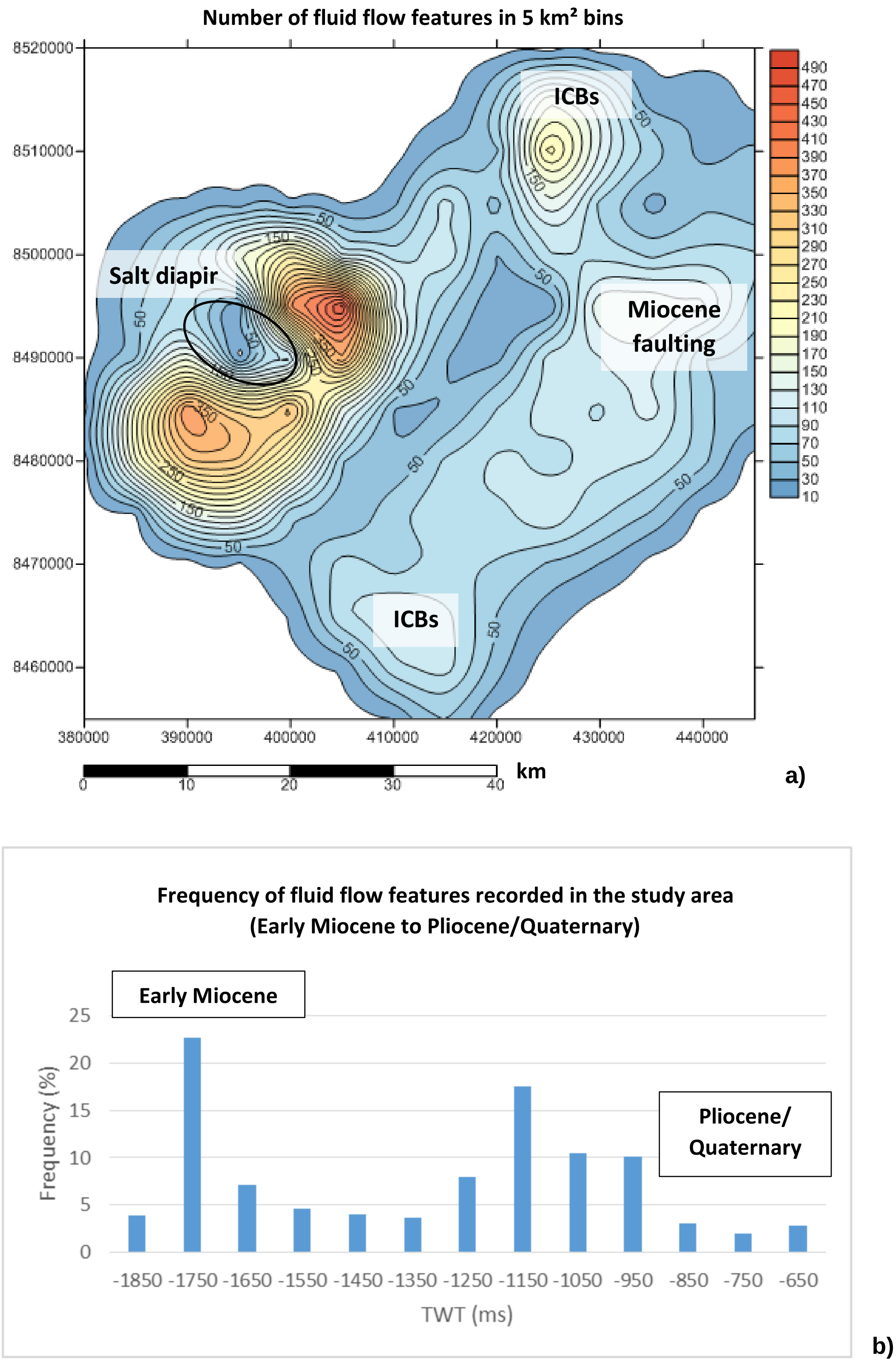
Number of fluid flow features in 5 km² bins
ICBs
Salt diapir
Miocene faulting
ICBs
km
a)
Frequency of fluid flow features recorded in the study area
(Early Miocene to Pliocene/Quaternary)
Early Miocene
Pliocene/ Quaternary
Frequency (%)
TWT (ms)
b)

Figure 23

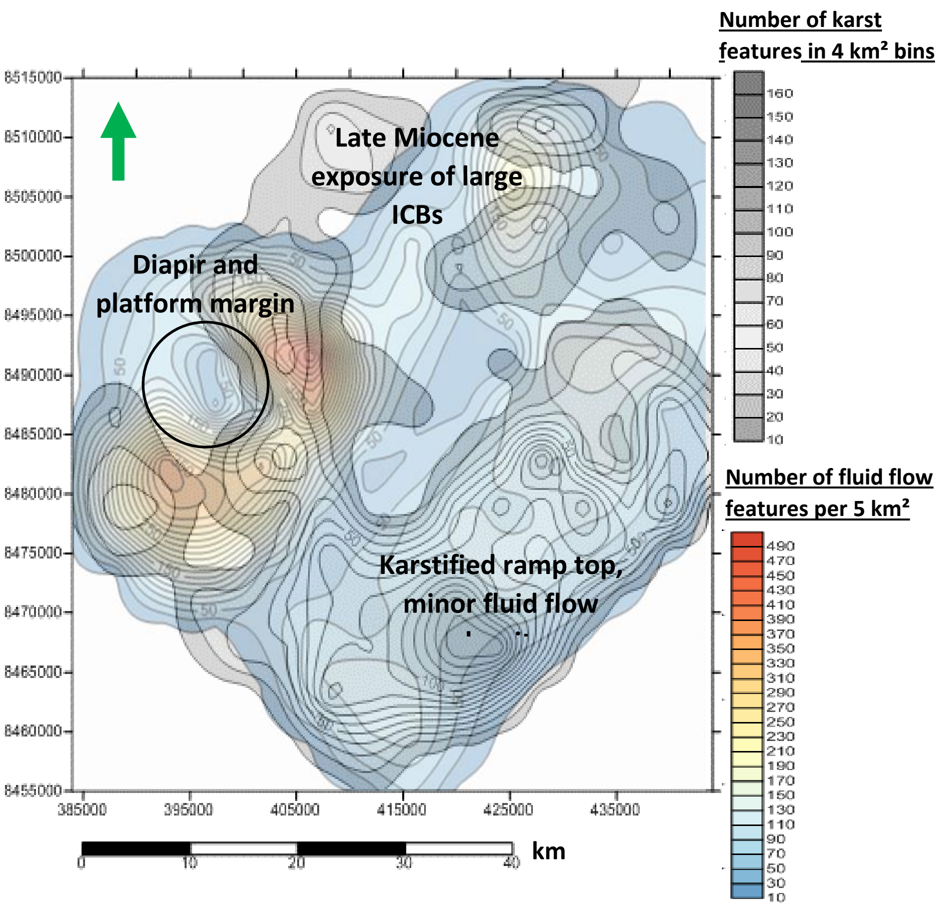

Number of karst features in 4 km² bins
160
150
140
130
120
110
100
90
80
70
60
50
40
30
20
10
Number of fluid flow features per 5 km²
490
470
450
430
410
390
370
350
330
310
290
270
250
230
210
190
170
150
130
110
90
70
50
30
10
Late Miocene exposure of large ICBs
Diapir and platform margin
Karstified ramp top, minor fluid flow
8515000
8510000
8505000
8500000
8495000
8490000
8485000
8480000
8475000
8470000
8465000
8460000
8455000
385000
395000
405000
415000
425000
435000
0
10
20
30
40
km


Figure 24

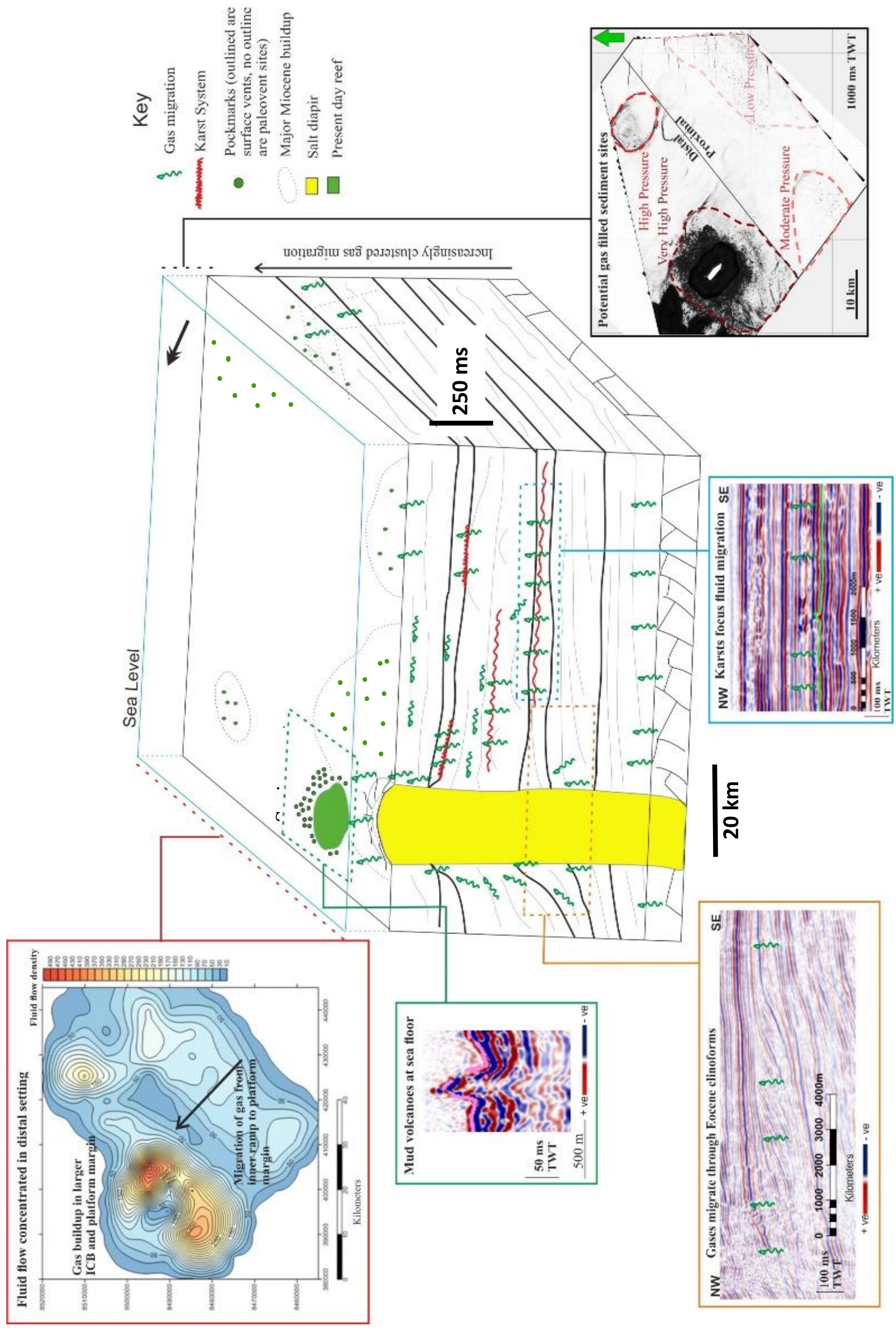
Key
Gas migration
Karst System
Pockmarks (outlined are surface vents, no outline are paleovent sites)
Major Miocene buildup
Salt diapir
Present day reef
Sea Level
Increasingly clustered gas migration
250 ms
20 km
Potential gas filled sediment sites
High Pressure
Very High Pressure
Moderate Pressure
Low Pressure
Proximal
Distal
10 km
1000 ms TWT
NW Karsts focus fluid migration SE
Mud volcanoes at sea floor
50 ms TWT
500 m
Gases migrate through Eocene clinoforms
NW
SE
Kilometers
Fluid flow concentrated in distal setting
Gas buildup in larger ICB and platform margin
Migration of gas from inner ramp to platform margin
Fluid flow density
Kilometers

Figure 25